Accelerated image reconstruction using extrapolated Tikhonov filtering for photoacoustic tomography

Sreedevi Gutta
Department of Computational and Data Sciences, Indian Institute of Science, Bangalore 560 012, India

Sandeep Kumar Kalva and Manojit Pramanik
School of Chemical and Biomedical Engineering, Nanyang Technological University, 62 Nanyang Drive, Singapore

Phaneendra K. Yalavarthy[a)]
Department of Computational and Data Sciences, Indian Institute of Science, Bangalore 560 012, India

(Received 17 October 2017; revised 23 April 2018; accepted for publication 17 May 2018; published 3 July 2018)

Purpose: Development of simple and computationally efficient extrapolated Tikhonov filtering reconstruction methods for photoacoustic tomography.
Methods: The model-based reconstruction algorithms in photoacoustic tomography typically utilize Tikhonov regularization scheme for the reconstruction of initial pressure distribution from the measured boundary acoustic data. The automated choice of regularization parameter in these cases is computationally expensive. Moreover, the Tikhonov scheme promotes the smooth features in the reconstructed image due to the smooth regularizer, thus leading to loss of sharp features. The proposed extrapolation method estimates the solution at zero regularization assuming the solution being a function of regularization parameter and thus posing it as a zero value problem. Thus, the numerically computed zero regularization solution is expected to have better features compared to standard Tikhonov solution, with an added advantage of removing the necessity of automated choice of regularization. The reconstructed results using this method were shown in three variants (Lanczos, traditional, and exponential) of Tikhonov filtering and were compared with the standard error estimate technique.
Results: Four numerical (including realistic breast phantom) and two experimental phantom data were utilized to show the effectiveness of the proposed method. It was shown that the proposed method performance was superior than the standard error estimate technique, being at least four times faster in terms of computation, and provides an improvement as high as 2.6 times in terms of standard figures of merit.
Conclusion: The developed extrapolated Tikhonov filtering methods overcome the difficulty of obtaining a suitable regularization parameter and shown to be reconstructing high-quality photoacoustic images with additional advantage of being computationally efficient, making it more appealing in real-time applications. [https://doi.org/10.1002/mp.13023]

Key words: extrapolation, image reconstruction, photoacoustic imaging, regularization, Tikhonov

1. INTRODUCTION

Photoacoustic tomography (PAT) is a noninvasive imaging modality that combines the advantages of optical absorption contrast and high spatial resolution.[1–4] In this modality, a short-pulsed laser beam irradiates the tissue causing an absorption of energy by the chromophores present in the tissue resulting in a small temperature rise. The increase in temperature results in emission of pressure waves (in the form of acoustic waves) due to thermoelastic expansion. The acoustic waves (also known as photoacoustic waves), thus generated, are collected using the ultrasound transducers placed on the surface of the tissue. The boundary acoustic measurements are utilized to reconstruct the initial pressure rise inside the tissue, which reveals the tissue pathophysiological state. Recently, PAT has extensively been applied for various biological applications such as brain imaging,[5–8] breast cancer imaging,[9] and blood vasculature imaging.[10–12]

Photoacoustic (PA) image reconstruction involves determination of initial pressure distribution, which maps to the absorbed energy, from the acoustic boundary measurements.[13,14] Several reconstruction algorithms exist, such as analytical and model-based, to solve this initial value problem.[13] Analytical algorithms, such as filtered back projection (FBP) and delay & sum, as well as time-reversal-based algorithms require large amount of data and their performance is limited in terms of providing the required quantitative information.[13] Recent emphasis has been on model-based image reconstruction algorithms, as they provide desired quantitative accuracy compared to these algorithms.[13,14] As the problem at hand is ill-conditioned, the computation of the approximate solution is difficult due to the severe error propagation (the detailed discussion is given in Appendix-B). Moreover, the most commonly deployed photoacoustic tomographic setups do not enclose the object, resulting in limited data (incomplete data) problem.[15] Furthermore, the number of imaging parameters (such as pixels in the reconstructed image) exceeding the measurements leads to these limited data problems, which make the reconstruction problem as ill-conditioned, necessitating the utilization of regularization in these model-based algorithms. This work is geared toward accelerating these model-based algorithms in limited data cases. The Tikhonov regularization is the most commonly utilized model-based image reconstruction algorithm in photoacoustic imaging.[13] An important step in Tikhonov regularization is to select an appropriate regularization parameter. It is well known that the reconstruction result is largely biased toward regularization parameter.[13,16] Moreover, the regularization parameter always filters some of the natural characteristics of the expected image. There have been attempts earlier to mitigate the effects of regularization via applying a deconvolution on top of the reconstruction step.[17,18] Several methods were proposed in the past, for determination of regularization parameter such as the Morozov discrepancy principle,[19] the Generalized Cross Validation (GCV),[20] and the L-curve method.[21] The discrepancy principle is the simplest method, to determine optimal regularization parameter, but it requires an estimation of noise in the experimental data and expected image. The GCV and L-curve methods do not require any prior information as discrepancy principle. Recently, a least-squares approach was developed and was shown to be an effective alternative compared to the L-curve and GCV methods for automatic selection of regularization parameter.[22] Subsequent to this work, an error estimate-based method was proposed and shown to be computationally efficient compared to the least-squares method in determining this regularization parameter automatically.[16] Despite all these developments, automated evaluation of regularization parameter is still computationally demanding and the metric for an automated choice of regularization parameter may not provide the desired reconstructed image characteristics as regularization inherently blurs the reconstructed image.[17,18] The ideal case will be to compute the regularization-free solution that does not have the blur (filtering of high frequencies) in the reconstructed image and is computationally efficient to deploy in real time.

In this work, an extrapolation method was proposed that helps to avoid the need of computing regularization parameter in an automated fashion.[23,24] As the solution is a function of regularization parameter (λ), one can accomplish this by extrapolating the solution at $\lambda = 0$, using the regularized solutions computed at several values of λ, thus even achieving the unbiasedness to the regularization parameter. In simple terms, we use the solution obtained at predetermined values of λ and extrapolate to find out the solution at $\lambda = 0$. It was shown (with an example problem) that the solution obtained at $\lambda = 0$ has the lowest error metrics, thus providing the optimal solution without adding significant computational burden. The extrapolation method was applied within the standard Tikhonov filtering method, namely Lanczos Tikhonov. The traditional Tikhonov and exponential filtering methods (details are given in Section IV) were also deployed here to show the versatility of the proposed method. The reconstruction results obtained from the proposed extrapolation method in these Tikhonov filtering reconstruction methods were compared with the results obtained from utilization of standard error estimate technique for evaluating regularization parameter in these methods. It was observed that the proposed method was computationally efficient, as it eliminates the burden of determining the regularization parameter explicitly and provides the desired reconstructed image characteristics. The reconstructed image quality was evaluated using the quantitative metrics such as error norm, Pearson correlation, contrast-to-noise ratio, universal image quality index, signal-to-noise ratio, and the residual norm (data-model misfit).

2. PHOTOACOUSTIC (PA) IMAGE RECONSTRUCTION

The mathematical model governing photoacoustic wave propagation can be written as[14]

$$\nabla^2 P(x,t) - \frac{1}{c^2}\frac{\partial^2 P(x,t)}{\partial t^2} = \frac{-\beta}{C_p}\frac{\partial H(x,t)}{\partial t}, \tag{1}$$

where $P(x,t)$ is the pressure at a point x and time t, c is the speed of sound in the medium, β is the thermal expansion coefficient, C_p is the specific heat, and $H(x,t)$ represents the energy deposited per unit time per unit volume. By solving Eq. (1), the acoustic information on the boundary of the imaging region can be obtained. This can be achieved by using finite elements,[25] finite difference,[26] pseudospectral methods,[27] or Green's function approach.[28] The PA reconstruction problem is to estimate the initial pressure that is $P(x,t)$ at $t = 0$ inside the imaging region, given the measured acoustic data on the boundary.

The forward model of PA imaging can be represented as linear system of equations, by using system matrix approach[18,22]

$$\mathbf{A}x = b, \tag{2}$$

where $\mathbf{A}$ is the system matrix containing impulse responses of all pixels in the imaging region as columns, b is the measured acoustic data on the boundary, and x is the initial pressure distribution. There are many approaches to solve for initial pressure such as filtered back projection (FBP), Fourier-domain reconstruction, and time-reversal methods.[13] These methods typically have a requirement of having large boundary data.[13,14] The model-based image reconstruction techniques are often sought after in limited data cases, which are more favorable in the experimental/clinical scenarios.

3. TIME REVERSAL METHOD

The main aim of PA image reconstruction is to estimate the initial pressure distribution from the measured boundary data. The k-wave time reversal is a computationally efficient method for estimation of initial pressure distribution, provided by an open-source k-wave toolbox.[27] The time-reversal method states that the PA solution $p(x,t)$ inside the imaging domain vanishes for $t > L$, where L indicates the longest time taken by the PA wave to pass through the domain.[18] The solution at $t = 0$, was obtained by imposing a zero initial condition at $t = L$ and the measured data as the boundary condition. The recorded data at discrete locations are interpolated to increase the input data to the reconstruction and have been shown in the case of time-reversal to improve the photoacoustic image reconstruction.[27] Note that the k-wave performs full-wave and time-reversal-based image reconstruction, and in this work, time-reversal method was utilized for comparison with the proposed method.

4. MODEL-BASED RECONSTRUCTION ALGORITHMS

4.A. Lanczos Tikhonov regularization method

The image reconstruction problem involves a cost function (Γ) to be minimized with respect to x in the least-squares sense

$$\Gamma = \|\mathbf{A}x - b\|_2^2, \tag{3}$$

where $\mathbf{A}$ is a $m \times n^2$ ill-conditioned system matrix, b denotes noisy measurement vector given as $b = \bar{b} + e$, with $\bar{b}$ being noise-free measurement and e denotes the noise in the measurement, and $\|.\|_2$ represents the ℓ_2 norm. The Tikhonov regularization changes the cost function to

$$\Gamma = (\|\mathbf{A}x - b\|_2^2 + \lambda\|\mathbf{L}x\|_2^2), \tag{4}$$

where λ is a regularization parameter and $\mathbf{L}$ is a regularization matrix. The closed-form solution can be obtained by minimizing the cost function in Eq. (4) resulting in,13,17

$$x_{Tik} = (\mathbf{A}^T\mathbf{A} + \lambda\mathbf{L}^T\mathbf{L})^{-1}\mathbf{A}^T b. \tag{5}$$

The properties of the solution depend on the choice of the regularization ($\mathbf{L}$ and λ). The standard (zeroth order) choice for $\mathbf{L}$ is identity matrix ($\mathbf{I}$); thus, the solution becomes[29]

$$x_{Tik} = (\mathbf{A}^T\mathbf{A} + \lambda\mathbf{I})^{-1}\mathbf{A}^T b. \tag{6}$$

These regularization methods involve matrix–matrix multiplications as well as solving large system of equations, which is computationally expensive. Therefore, the Tikhonov regularization was implemented in a Lanczos bidiagonalization framework, to reduce the computational complexity.[16,18,22] The Lanczos bidiagonalization of the system matrix $\mathbf{A}$ can be written as[22,30]

$$\mathbf{M}_{q+1}(\beta_1 e_1) = b \tag{7}$$

$$\mathbf{A}\mathbf{R}_q = \mathbf{M}_{q+1}\mathbf{B}_q \tag{8}$$

$$\mathbf{A}^T\mathbf{M}_{q+1} = \mathbf{R}_q\mathbf{B}_q^T + \alpha_{q+1} r_{q+1} e_{q+1}^T \tag{9}$$

where $\mathbf{M}_q = [m_1, m_2, \ldots, m_q]$ and $\mathbf{R}_q = [r_1, r_2, \ldots, r_q]$ are the left and right orthogonal Lanczos matrices of dimensions $m \times (q+1)$ and $n^2 \times q$ respectively. The r_i's in the $\mathbf{R}_q$ are the normalized residual vectors at Lanczos iteration "i".[31] The $\mathbf{B}_q$ is the lower bidiagonal matrix of dimension $(q+1) \times q$ with α_q in the main diagonal and β_q in the lower subdiagonal, β_1 is the ℓ_2 norm of b, and e_q is a unit vector of dimension $q \times 1$. Using the above Lanczos bidiagonalization, Eq. (6) reduces to[22]

$$x^{(q)} = (\mathbf{B}_q^T\mathbf{B}_q + \lambda\mathbf{I})^{-1}\beta_1\mathbf{B}_q^T e_1; \quad x_{Lanc} = \mathbf{R}_q x^{(q)}. \tag{10}$$

This method requires a suitable number of Lanczos iterations and value of the regularization parameter to be chosen and we achieve these using error estimate-based method, which was proven to be computationally efficient.[16] It is briefly reviewed here for completeness. The family of error estimate as proposed in Refs. [32,33], is given as

$$\|e\|_2^2 \approx \eta_v^2 := e_o^{v-1} e_1^{5-2v} e_2^{v-3}, \quad v \in \mathbb{R} \tag{11}$$

with

$$e_o := \|r\|_2^2, \quad e_1 := \|A^T r\|_2^2, \quad e_2 := \|AA^T r\|_2^2, \text{ and} \tag{12}$$

$r = b - \mathbf{A}x$ represents the residue (data-model misfit). The error estimate for $v = 2$ can be expressed as

$$\eta_2 = \frac{\|r\|_2\|\mathbf{A}^T r\|_2}{\|\mathbf{A}\mathbf{A}^T r\|_2}. \tag{13}$$

The algorithm to achieve this consists of two phases. In the first phase, one determines the required number of Lanczos iterations at a suboptimal regularization value. The regularization parameter is refined in the second phase by fixing the number of Lanczos iterations. Interested readers can refer to Algorithm-1 in Ref. [16], for a detailed description of the algorithm.

4.A.1. The proposed extrapolated Lanczos Tikhonov method

The actual minimization one wishes to perform is on cost function given by Eq. (3), which does not involve λ. Due to the ill-conditioned nature of the problem, one has to introduce the regularization functional to stabilize the solution. One way to obtain the solution at $\lambda = 0$ is to perform an extrapolation given x at multiple values of λ (assuming that the solution is a function of λ, which is true for any regularization scheme). Thus, the extrapolation method avoids the difficulty of evaluating the regularization parameter in an automated fashion, which is computationally demanding.[16,23,24]

Let the singular value decomposition (SVD) of the bidiagonal matrix (which can be obtained in $\mathcal{O}(n^2)$ operations) be

$$\mathbf{B}_q = \hat{\mathbf{U}}\hat{\mathbf{S}}\hat{\mathbf{V}}^T, \tag{14}$$

where $\hat{\mathbf{U}} = (\widehat{U_1}, \widehat{U_2}, \ldots, \widehat{U_q})$ and $\hat{\mathbf{V}} = (\hat{V}_1, \hat{V}_2, \ldots, \hat{V}_q)$ are orthogonal matrices and $\hat{\mathbf{S}}$ is a diagonal matrix with diagonal entries $\hat{S}_1 \geq \hat{S}_2..... > 0$. The solution given in Eq. (10) can be rewritten in terms of SVD of $\mathbf{B}_q$ as

$$\begin{aligned} x^{(q)} &= (\hat{\mathbf{V}}\hat{\mathbf{S}}^T\hat{\mathbf{S}}\hat{\mathbf{V}}^T + \lambda\mathbf{I})^{-1}\beta_1\hat{\mathbf{V}}\hat{\mathbf{S}}^T\hat{\mathbf{U}}^T e_1 \\ &= \sum_{i=1}^{q}\frac{\hat{S}_i^2}{\hat{S}_i^2+\lambda}\frac{<\hat{U}_i,\beta_1 e_1>}{\hat{S}_i}\hat{V}_i; \\ x_{Lanc,\lambda} &= \mathbf{R}_q x^{(q)} \end{aligned} \tag{15}$$

where $< .,. >$ represents the inner product operation of the argument vectors. Using pairwise orthogonality of R_q, Eq. (15) can be written as

$$\mathbf{R}_q^T x_{Lanc,\lambda_j} = \sum_{i=1}^{q}\frac{\hat{S}_i^2}{\hat{S}_i^2+\lambda_j}\frac{<\hat{U}_i,\beta_1 e_1>}{\hat{S}_i}\hat{V}_i, \tag{16}$$

where $i = 1,...q$ and λ_j is the jth value in the series of λ's that can provide meaningful solutions (x). Rearranging Eq. (16), we obtain

$$\frac{<\hat{U}_i,\beta_1 e_1>}{\hat{S}_i}\hat{V}_i = \frac{\hat{S}_i^2+\lambda_j}{\hat{S}_i^2}\mathbf{R}_q^T x_{Lanc,\lambda_j} \quad j = 1,2...p \tag{17}$$

with p denoting the total number of λ values. Summing the above equation for given values of j,

$$\frac{<\hat{U}_i,\beta_1 e_1>}{\hat{S}_i}\hat{V}_i = \frac{1}{p}\left[\sum_{j=1}^{p}\left(1+\frac{\lambda_j}{\hat{S}_i^2}\right)\mathbf{R}_q^T x_{Lanc,\lambda_j}\right]. \tag{18}$$

The solution at $\lambda = 0$ is obtained by substituting Eq. (18) in Eq. (15),

$$x_{Lanc}^{e} = \sum_{i=1}^{q}\frac{1}{p}\left[\sum_{j=1}^{p}\left(1+\frac{\lambda_j}{\hat{S}_i^2}\right)\mathbf{R}_q\mathbf{R}_q^T x_{Lanc,\lambda_j}\right], \tag{19}$$

where the super fix e denotes the extrapolated Lanczos Tikhonov solution at $\lambda = 0$. The results presented in this work were obtained by considering five λ values (i.e., $p = 5$) as proposed in Ref. [24]. Note that choosing less than five values were proven to be suboptimal for the ill-posed problems, like the one at hand.

$$\begin{aligned} &\lambda_1 = \alpha, \quad \lambda_2 = 10^{-2}\alpha, \quad \lambda_3 = \frac{\alpha+\beta}{2}, \\ &\lambda_4 = 10^2\beta, \quad \lambda_5 = \beta. \end{aligned} \tag{20}$$

The values α and β were chosen as 1 and $1e{-}10$, respectively, for the presented results.

4.B. Traditional Tikhonov regularization

The Lanczos Tikhonov will be equivalent to the traditional Tikhonov regularization when the number of bidiagonal iterations q is equal to the column space of system matrix (**A**). Although we have provided the Lanczos framework for the proposed method, for completeness, the traditional Tikhonov regularization was also introduced and utilized in this work. The SVD of the system matrix **A** can be written as

$$\mathbf{A} = \mathbf{U}\mathbf{S}\mathbf{V}^{\mathbf{T}}, \tag{21}$$

where **U** and **V** are orthogonal matrices and **S** is a diagonal matrix with increasing sequence of diagonal entries $S_1 \geq S_2..... > 0$. The solution given in Eq. (6) can be rewritten using the SVD of **A** as[29]

$$x_{Tik} = \mathbf{V}\mathbf{S}^{\dagger}\mathbf{U}^T b, \tag{22}$$

where

$$\mathbf{S}^{\dagger} = diag\left(\frac{F_i}{S_i}\right), \tag{23}$$

with the filter factors F_i being

$$F_i = \frac{S_i^2}{S_i^2+\lambda}. \tag{24}$$

Therefore, the Tikhonov solution with the filter factors become[29]

$$x_{Tik} = \sum_{i=1}^{k}\frac{S_i^2}{S_i^2+\lambda}\frac{<U_i,b>}{S_i}V_i, \tag{25}$$

where $k = min(m,n^2)$ with $< .,. >$ representing the inner product operation of the argument vectors.

As stated earlier, the automatic choice of regularization parameter was performed using the method of error estimate, given in detail for photoacoustic tomography in Ref. [16]. For completeness, this is briefly reviewed here.

The regularization parameter (λ) can be determined by starting with an equally spaced grid of values chosen in the interval between [λ_{min},λ_{max}] with λ_{min} and λ_{max} being $1e{-}10$ and 1, respectively. Then, for each value of λ, the regularized solution and error estimate are computed. The parameter λ, which minimizes the error estimate given in Eq. (13), was chosen to be the regularization parameter. To improve the accuracy of the obtained λ, more points are added around the chosen λ using bisection method, until the distance between adjacent points is less than the predefined value (1e-4). In this work, SVD was computed using "csvd", which is a Matlab routine in the regularization toolbox.[34]

4.B.1. The proposed extrapolated Tikhonov method

Using the concept of orthogonality, Eq. (25) can be written as

$$\frac{<U_i,b>}{S_i} = \frac{S_i^2+\lambda_j}{S_i^2}<x_{\lambda_j},V_i> \quad j = 1,2...p \tag{26}$$

with p denoting the total number of λ values that can be considered (ranging from minimum of 2 to k; in this work, it is 5). Summing Eq. (26) for all values of j, the relation can be reexpressed as

$$\frac{<U_i,b>}{S_i} = \frac{1}{p}<\sum_{j=1}^{p}\left(1+\frac{\lambda_j}{S_i^2}\right)x_{\lambda_j},V_i>. \tag{27}$$

The solution at $\lambda = 0$ is obtained by substituting Eq. (27) in Eq. (25),

$$x^e_{Tik} = \sum_{i=1}^{k} \frac{1}{p} < \sum_{j=1}^{p} \left(1 + \frac{\lambda_j}{S_i^2}\right) x_{\lambda_j}, V_i > V_i. \tag{28}$$

where the super fix e represents the solution of extrapolated Tikhonov corresponding to $\lambda = 0$. Note that the solution obtained in this way corresponds to the approximate solution obtained by minimizing the cost function given in Eq. (3). The solution can also be obtained without computing the SVD of the system matrix and the mathematical framework is given in Appendix A. A flowchart showing important steps performed in the proposed scheme as well as standard Tikhonov method is given in Fig. 1 for easy following. The detailed comparison of characteristics of solutions using unregularized least squares, Tikhonov, and extrapolated Tikhonov methods was discussed in Appendix B. The difference between these methods was also clearly brought out in the same Appendix.

4.C. Exponential filtering

The exponential filtering was recently proposed technique for photoacoustic imaging as a generalization of the Tikhonov method.[29] The filter factors [in Eq. (23)] for exponential filtering are given as

$$F_i = 1 - exp\left(\frac{-S_i^2}{\lambda}\right). \tag{29}$$

The regularized exponential filtering solution using the filter factors thus become[29]

$$x_{Exp} = \sum_{i=1}^{k} \left[1 - exp\left(\frac{-S_i^2}{\lambda}\right)\right] \frac{< U_i, b >}{S_i} V_i. \tag{30}$$

The exponential filtering and Tikhonov filter factors become equal when $S_i^2 << \lambda$, logically making exponential filtering perform as an asymptotic regularization. The spectral filtering methods discussed so far, Tikhonov and exponential filtering has a major limitation in terms of

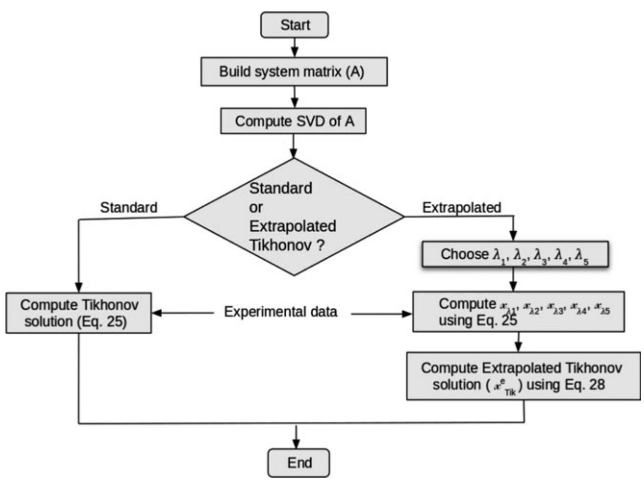

FIG. 1. Flowchart showing the major steps for standard Tikhonov and extrapolated Tikhonov methods discussed in Section 4.B.

computation of SVD of system matrix, which is of $\mathcal{O}(m * n^4)$ complexity, but the decomposition can be performed *a-priori* and can be seen as a one-time overhead for a fixed data collection geometry.

The suitable regularization parameter λ in case of exponential filtering method can be chosen in a similar way as Tikhonov method. The only difference is that the exponential filter factors are used instead of Tikhonov filter factors, while computing the regularized solution (details are given in Ref. [16]).

4.C.1. *The proposed extrapolated exponential filtering method*

The Eq. (30) can be rewritten using the orthogonality property of V_i as

$$< x_\lambda, V_i > \; = \sum_{i=1}^{k} \left[1 - exp\left(\frac{-S_i^2}{\lambda}\right)\right] \frac{< U_i, b >}{S_i}, \tag{31}$$

The notation is similar to the one utilized in Section 4.B.1. Rearranging Eq. (31), we obtain

$$\frac{< U_i, b >}{S_i} = \frac{1}{1 - exp\left(\frac{-S_i^2}{\lambda_j} s\right)} < x_{\lambda_j}, V_i > \quad j = 1, 2 \ldots p \tag{32}$$

where p represents the total number of λ values (in here also it is 5). Summing the relation in Eq. (32) for all values of j, the equation can be rewritten as

$$\frac{< U_i, b >}{S_i} = \frac{1}{p} < \sum_{j=1}^{p} \frac{1}{1 - exp\left(\frac{-S_i^2}{\lambda_j}\right)} x_{\lambda_j}, V_i > . \tag{33}$$

The solution at $\lambda = 0$ is obtained by substituting Eq. (27) in Eq. (25),

$$x^e_{Exp} = \sum_{i=1}^{k} \frac{1}{p} < \sum_{j=1}^{p} \frac{1}{1 - exp\left(\frac{-S_i^2}{\lambda_j}\right)} x_{\lambda_j}, V_i > V_i. \tag{34}$$

5. PERFORMANCE METRICS/FIGURES OF MERIT

The following performance metrics were utilized to evaluate the quantitative accuracy of the reconstructed photoacoustic images.

5.A. Residual norm

Residual norm (also known as data-model misfit) is a measure of discrepancy of the expected solution from the computed solution. It is defined as

$$Residue(R) = \|b - \mathbf{A}x_{recon}\|_2. \tag{35}$$

In real clinical scenarios, the expected x is unknown; thus, the residue is a good measure of tractability of the computed solution.

5.B. Error norm

Error norm (also known as reconstruction error) measures the deviation of the reconstructed image from the expected target image. It is expressed as

$$Err(x, x_{recon}) = \|x - x_{recon}\|_2 \tag{36}$$

where x and x_{recon} corresponds to the target and the reconstructed image, respectively. This provides a measure of how close is the reconstructed solution with respect to the expected one. The lower the value better is the performance of the reconstruction algorithm.

5.C. Pearson correlation (PC)

Pearson correlation (PC) is a quantitative metric to measure the degree of correlation between the expected and the reconstructed image.[16,35] It is defined as

$$PC(x, x_{recon}) = \frac{cov(x, x_{recon})}{\sigma_x \sigma_{x_{recon}}} \tag{37}$$

where x is the expected initial pressure distribution, x_{recon} is the reconstructed initial pressure distribution, cov is the covariance, and σ represents the standard deviation. The value of PC ranges from -1 to 1. Higher value of PC indicates better detectability of the targets in the reconstructed image.

5.D. Contrast to noise ratio (CNR)

Contrast to Noise Ratio (CNR) is an another performance metric, which is defined as[16]

$$CNR = \frac{\mu_{roi} - \mu_{back}}{(\sigma_{roi}^2 a_{roi} + \sigma_{back}^2 a_{back})^{1/2}} \tag{38}$$

where μ denotes the mean and σ represents the standard deviation. The "*roi*" and "*back*" represent the region of interest and the background correspondingly in the reconstructed image. The area ratio is represented as $a_{roi} = \frac{A_{roi}}{A_{total}}$ and $a_{back} = \frac{A_{back}}{A_{total}}$. Higher value of CNR indicates better the differentiability of the region of interest from the background.

5.E. Universal image quality index (UIQI)

Universal Image Quality Index (UIQI) is a quantity defined to measure the distortion in the reconstructed image. It is defined as[36]:

$$UIQI = \frac{4\ cov(x, x_{recon})\mu_x \mu_{x_{recon}}}{(\sigma_x^2 + \sigma_{x_{recon}}^2)(\mu_x^2 + \mu_{x_{recon}}^2)} \tag{39}$$

It can be observed that this measure is a combination of three factors: correlation coefficient to measure the degree of correlation, luminance distortion to measure the closeness of mean luminance, and contrast distortion to measure the similarity of contrasts in the target and the reconstructed images.

5.F. Signal-to-noise ratio (SNR)

The computation of above figures of merit, excluding the residue norm, requires one to know the expected target image (x). In experimental cases, the x is unknown, the figure of merit that was utilized to quantify the reconstruction performance was signal-to-noise ratio (SNR). It can be written as

$$SNR(dB) = 20 \times log_{10}\left(\frac{S}{n}\right), \tag{40}$$

where S indicates the peak-to-peak signal amplitude and n denotes the standard deviation of the background.

6. NUMERICAL AND EXPERIMENTAL EVALUATIONS

6.A. Numerical phantoms evaluation

Four numerical phantoms were considered with three of them having unipolar (binary) distributions of initial pressure, to prove the efficacy of the proposed method. A numerical blood vessel phantom [shown in Fig. 2(a)] with initial pressure rise of 1 kPa was used, as photoacoustic imaging is widely used for visualizing internal blood vessel structures. A Derenzo phantom consisting of small and large target distributions was also chosen as shown in Fig. 2(b). A target with alphabets "PAT" [shown in Fig. 2(c)] was used for evaluating the performance of the proposed method in reconstructing sharp edges. To further evaluate the ability of the proposed method, a realistic numerical breast phantom created from contrast-enhanced magnetic resonance (MR) imaging data was considered.[37,38] This phantom facilitates more realistic simulations, as they closely represent patient anatomical structures. A YZ slice of the right breast of a healthy volunteer, having dimension of 374 × 460 × 712 was shown in Fig. 2(d). The considered slice of the numerical breast

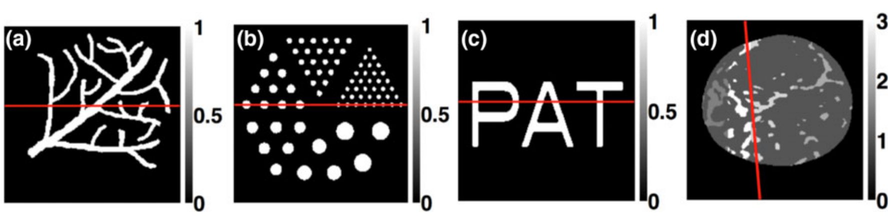

FIG. 2. Numerical phantoms used in this work (a). Blood vessel phantom, (b). Derenzo phantom, (c). PAT phantom, (d). Realistic breast phantom. [Color figure can be viewed at wileyonlinelibrary.com]

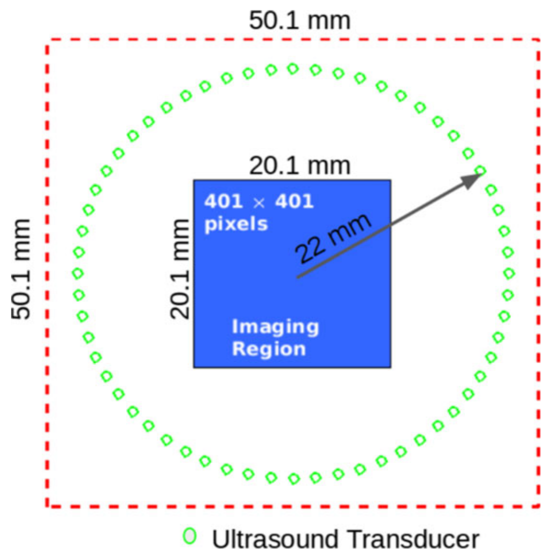

FIG. 3. Schematic of the photoacoustic data acquisition setup. Detectors are placed in equispaced circular fashion around imaging domain (shaded region). The number of pixels considered for the computational grid is specified in the top left corner of the imaging region. [Color figure can be viewed at wileyonlinelibrary.com]

phantom has varying initial pressure distribution from 0 to 3, in contrast to the numerical phantoms which have only binary initial pressure distribution.

The computational domain having 401 × 401 pixels spanning 20.1 × 20.1 mm was considered (also shown in Fig. 3). The acoustic data were generated on a 401 × 401 grid using an open source k-wave toolbox[27] and the reconstructions were done on a 201 × 201 grid. To mimic the experimental data, the collected data were added with 1% white gaussian noise, having a signal-to-noise (SNR) ratio of 40 dB. Sixty detectors that are equispaced, having a center frequency of 2.25 MHz, and 70% bandwidth were placed on the surface of the imaging region of radius 22 mm. The data were recorded for a total of 512 time steps with a step size 50 ns. The medium was assumed to be homogeneous, having speed of sound as 1500 m/s, with no absorption and dispersion. The system response for all pixels, to be filled in the corresponding columns of matrix **A** were obtained using the Green's function, which is an impulse response of the system. For the simulations presented in this work, the Green's function involving Hankel function of the first kind of order zero was utilized to generate the impulse response.[28] Note that in all simulations, data were collected on a higher dimensional grid (401 × 401) and reconstructions were performed on a lower dimensional grid (201 × 201). The schematic of the acquisition setup was shown in Fig. 3, with imaging domain indicated as a shaded region. A Linux workstation with dual six-core Intel Xeon processor having a speed of 2.66 GHz

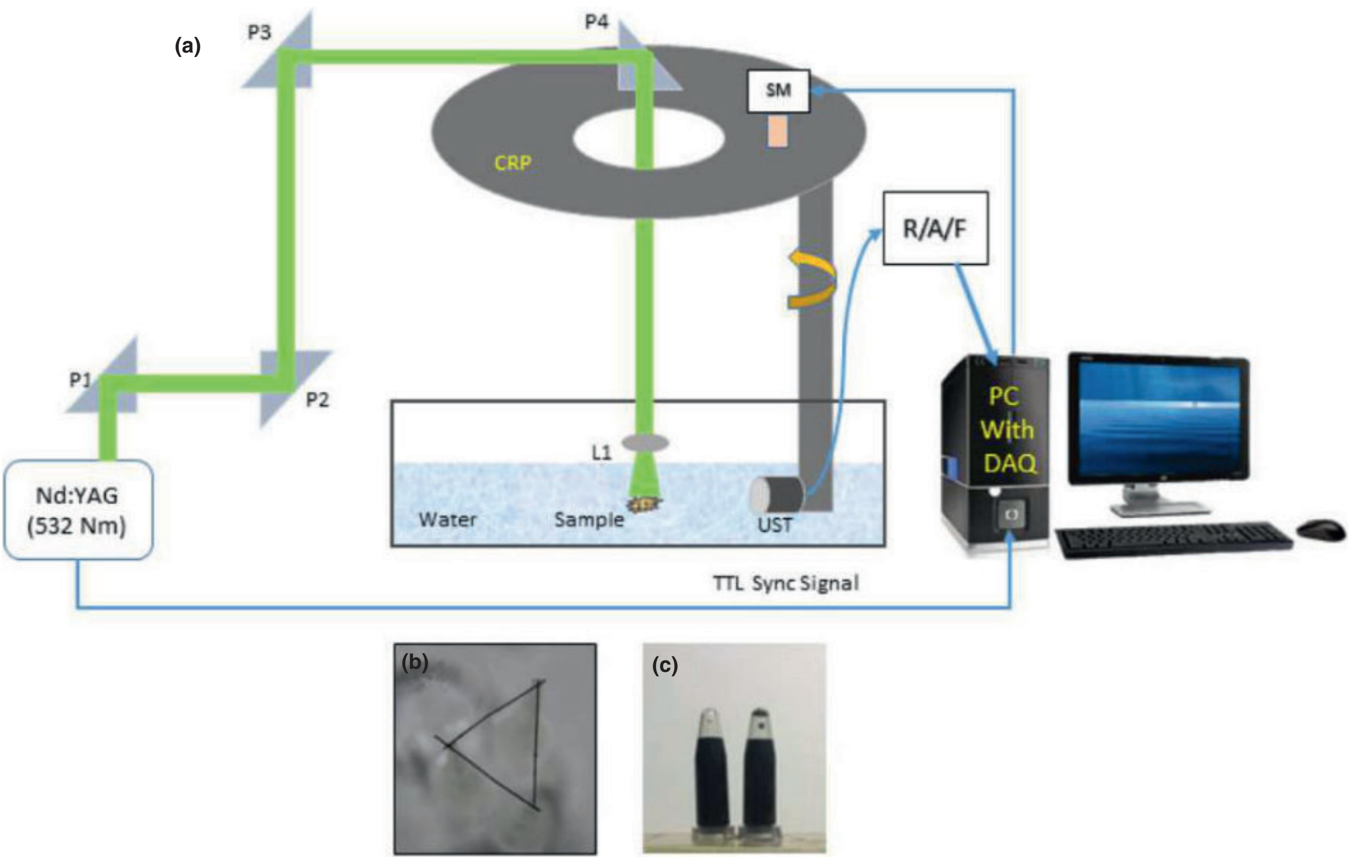

FIG. 4. (a) Schematic showing the major components of experimental system used for photoacoustic data acquisition CRP: Circular rotating plate, SM: Stepper motor, P1,P2,P3,P4: Uncoated right-angled prisms, L1: Plano-concave lens, R/A/F: Receiver, Amplifier, and Filter for photoacoustic signal, DAQ: Data Acquisition Card, UST: Ultrasound Transducer. (b) Photograph of triangular-shaped horse hair phantom. (c) Photograph of circular-shaped tubes filled with Indian black ink that were used in this work. [Color figure can be viewed at wileyonlinelibrary.com]

with 64 GB RAM was used for all the computations performed in this work.

6.B. Experimental phantoms evaluation

The experiment was conducted using the imaging system shown in Fig. 1(a) similar to Fig. 1(e) of Ref. [39]. A Q-switched Nd:YAG-pulsed laser (Continuum, Surelite Ex) capable of delivering 532 nm wavelength light of 5 ns duration and 10 Hz repetition rate was utilized. Laser pulses were delivered to the sample using four right-angle uncoated prisms (PS911, Thorlabs) and one uncoated Plano-concave lens L1 (LC1715, Thorlabs). The energy density on the phantom was ~ 9 mJ/cm^2, within ANSI safety limit (20 mJ/cm^2).[40] To experimentally evaluate the proposed method, a triangular-shaped horse hair phantom [Fig. 4(b)] and circular-shaped ink-tube phantom [Fig. 4(c)] were used. The horse hair diameter and side length were ~ 0.15 and ~ 10 mm, respectively, and was glued to the pipette tips adhered on acrylic slab.[41] The circular-shaped phantom was made using low-density polyethylene (LDPE) tubes having 5 mm inner diameter and filled with black Indian ink. The tubes were affixed at the bottom of the acrylic slab and placed in PAT scanner at 0 and 15 mm from the scanning center. The photoacoustic data were collected around these phantoms in full 360 degree using a 2.25 MHz flat ultrasound transducer (Olympus-NDT, V306-SU) of 13 mm diameter active area and $\sim 70\%$ nominal bandwidth. The distance from the center of the PAT scanner to the face of the ultrasonic transducer was 37.02 mm for horse hair phantom and 38.22 mm for tube phantom. The detected PA signals were preprocessed (amplification and filtration) using a pulse amplifier (Olympus-NDT, 5072PR) and then saved using a data acquisition (DAQ) card (GaGe, compuscope 4227) inside a windows 10 desktop system having Intel Xeon 3.7 GHz 64-bit processor and 16 GB RAM. Sync signal from laser was used to synchronize the data acquisition with laser illumination. Even though the data were collected using a sampling frequency of 25 MHz, simulations were performed at a rate of 12.5 MHz (as we have considered only 512 time samples alternatively from the detected 1024 samples). The reconstruction region consists of 200 $\times$ 200 pixels on a size of 40 $\times$ 40 mm. The dimension of the system matrix built for this geometry was 51,200 $\times$ 40,000: 51,200 corresponds to 512 time samples each of 100 detectors and 40,000 corresponds to the total number of pixels in

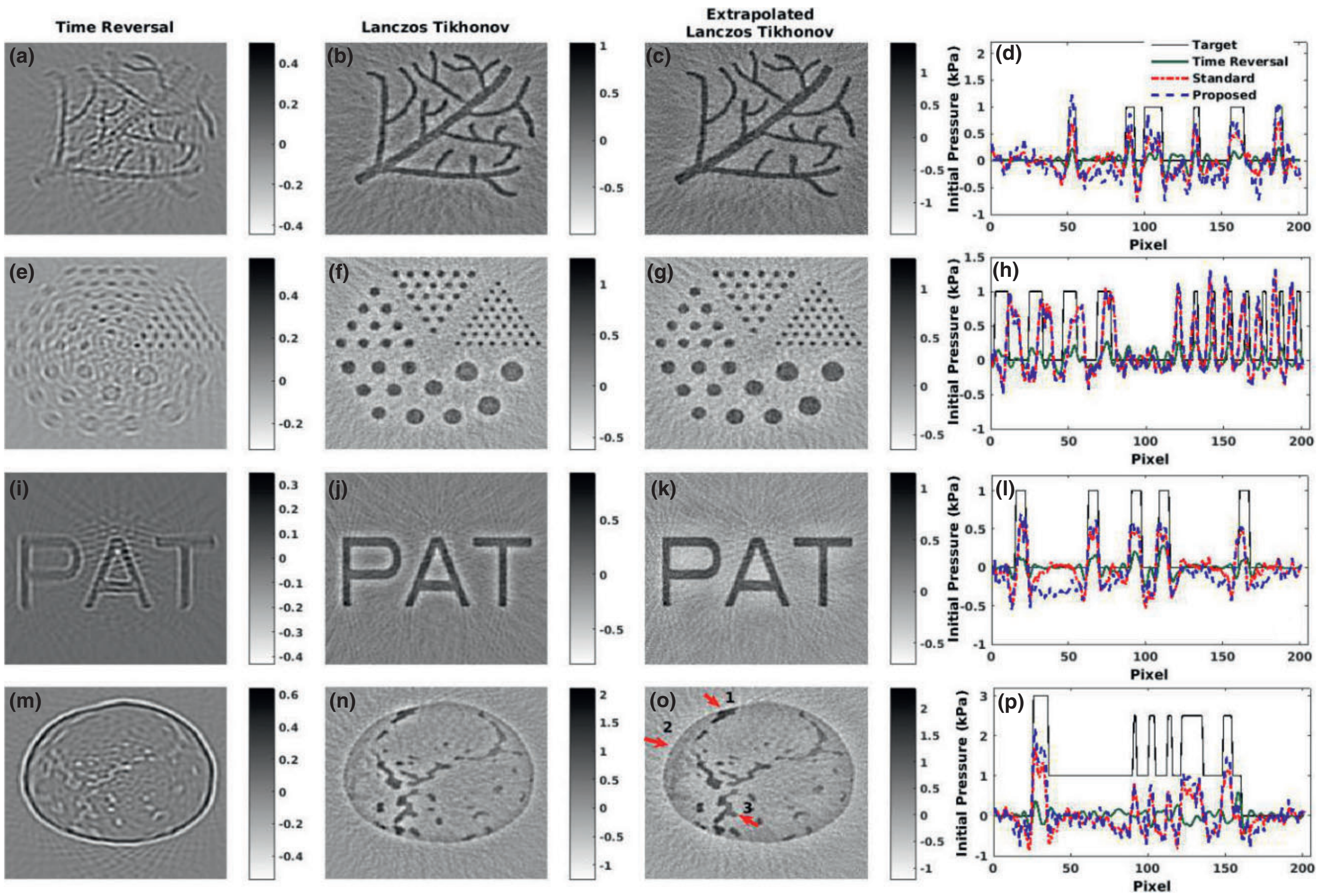

FIG. 5. Reconstructed images for Lanczos Tikhonov regularization discussed in Section 4.A using time-reversal (a,e,i,m), standard error estimate (b,f,j,n) and proposed extrapolated Lanczos Tikhonov method (c,g,k,o). A one-dimensional profile plot for the reconstructed images along the line in numerical phantoms was shown in (d,h,l,p). The residual norm and performance metrics corresponding to these reconstruction results were given in Fig. 6. [Color figure can be viewed at wileyonlinelibrary.com]

the imaging grid. The ground truth for these experimental cases is hard to determine and therefore is not available.

7. RESULTS

The reconstructed initial pressure distribution for blood vessel phantom [Fig. 2(a)] using time reversal (discussed in Section III), error estimate in Lanczos Tikhonov method, and proposed extrapolated Lanczos Tikhonov method (discussed in Section 4.A) were shown in Figs. 5(a), 5(b), and 5(c), respectively. A one-dimensional profile plot for the reconstructed results along the line in the target blood vessel phantom [as given in Fig. 2(a)] was shown in Fig. 5(d). It is evident from these results that the time-reversal method performance is poor compared to other methods due to the available data being limited. As this work mainly focused on utilizing the limited data, for rest of this work, the time-reversal method was not considered as a standard method for evaluating the reconstruction performance. From profile plot, it can be seen that the quantitative accuracy of reconstructed image using proposed method was superior to error estimate. The residual norm and performance metrics of these reconstructions were shown in Fig. 6. The typical computation time taken for both the methods was given in Table I. The

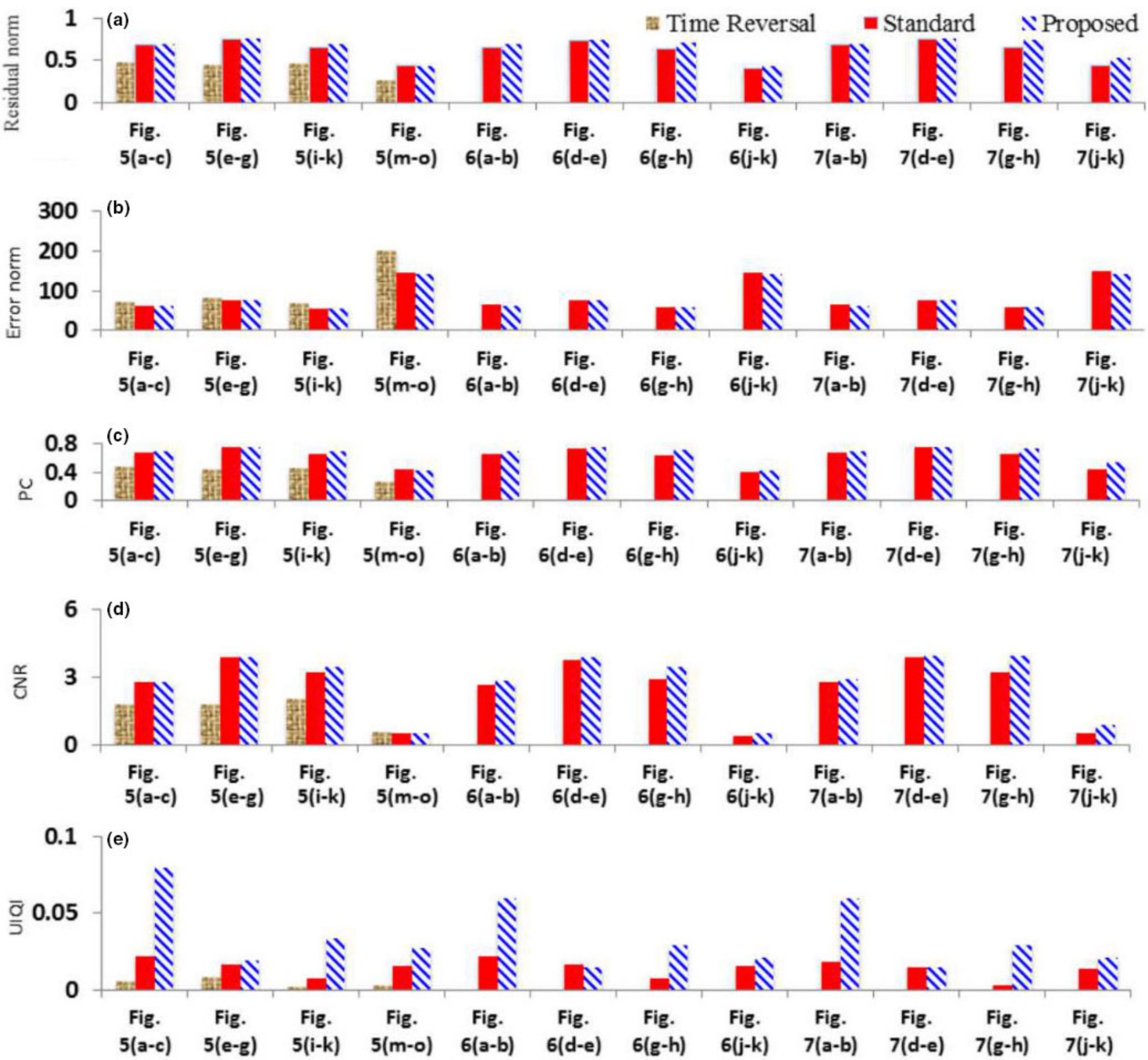

FIG. 6. For the reconstructed results presented in Figs. 5, 7, 8, the figures of merit (a). Residual norm (Section 5.A) (the lesser value indicates better reconstruction performance), (b). Error norm or reconstruction error (Section 5.A) (the lesser value indicates better reconstruction performance), (c). Pearson Correlation (Section 5.C) (the higher value indicates better reconstruction performance), (d). Contrast to noise ratio (Section 5.D) (the higher value indicates better reconstruction performance), and (e). Universal image quality index (Section 5.E) (the higher value indicates better reconstruction performance). [Color figure can be viewed at wileyonlinelibrary.com]

TABLE I. Computational time (in seconds) for the reconstruction results shown in Figs. 5, 7, 8, and 9. One-time computation of building the system matrix (116 s, applicable to all methods) and SVD (300.7 min, applicable to only Tikhonov and exponential filtering) was excluded.

Figure	Method	Phantom (detectors)	Standard (error estimate)	Proposed (extrapolation)
5(b) and 5(c)	Lanczos Tikhonov	Blood vessel (60)	116.83	28.49
7(a) and 7(b)	Tikhonov	Blood vessel (60)	312.23	73.91
8(a) and 8(b)	Exponential filtering	Blood vessel (60)	310.79	72.63
9(a) and 9(b)	Lanczos Tikhonov	Horse hair (100)	140.61	26.03
9(d) and 9(e)	Tikhonov	Horse hair (100)	330.37	65.27
9(g) and 9(h)	Exponential filtering	Horse hair (100)	344.17	65.17

system matrix building time ($\sim$ 116 s) was excluded from the computation time reported in Table I. From Table I, it was evident that the proposed method was four times computationally faster than the standard method (error estimate). The reconstruction results for the Derenzo phantom [Fig. 2(b)] were shown in Figs. 5(e), 5(f), and 5(g), with the profile plot shown in Fig. 5(h). Similar trend as observed earlier for the blood vessel phantom was followed for the Derenzo phantom. Reconstruction results pertaining to "PAT" phantom were presented in Figs. 5(i), 5(j), and 5(k), with the profile plot along the line given in Fig. 2(c) was shown in Fig. 5(l). The reconstruction results using time reversal, error estimate in Lanczos Tikhonov method, and proposed extrapolation methods for the numerical breast phantom were shown in Figs. 5(m), 5(n), and 5(o), respectively. Red arrows numbered 1 and 3 in Fig. 5(o) indicate that the proposed extrapolation method was able to reconstruct varying initial pressure distribution better than

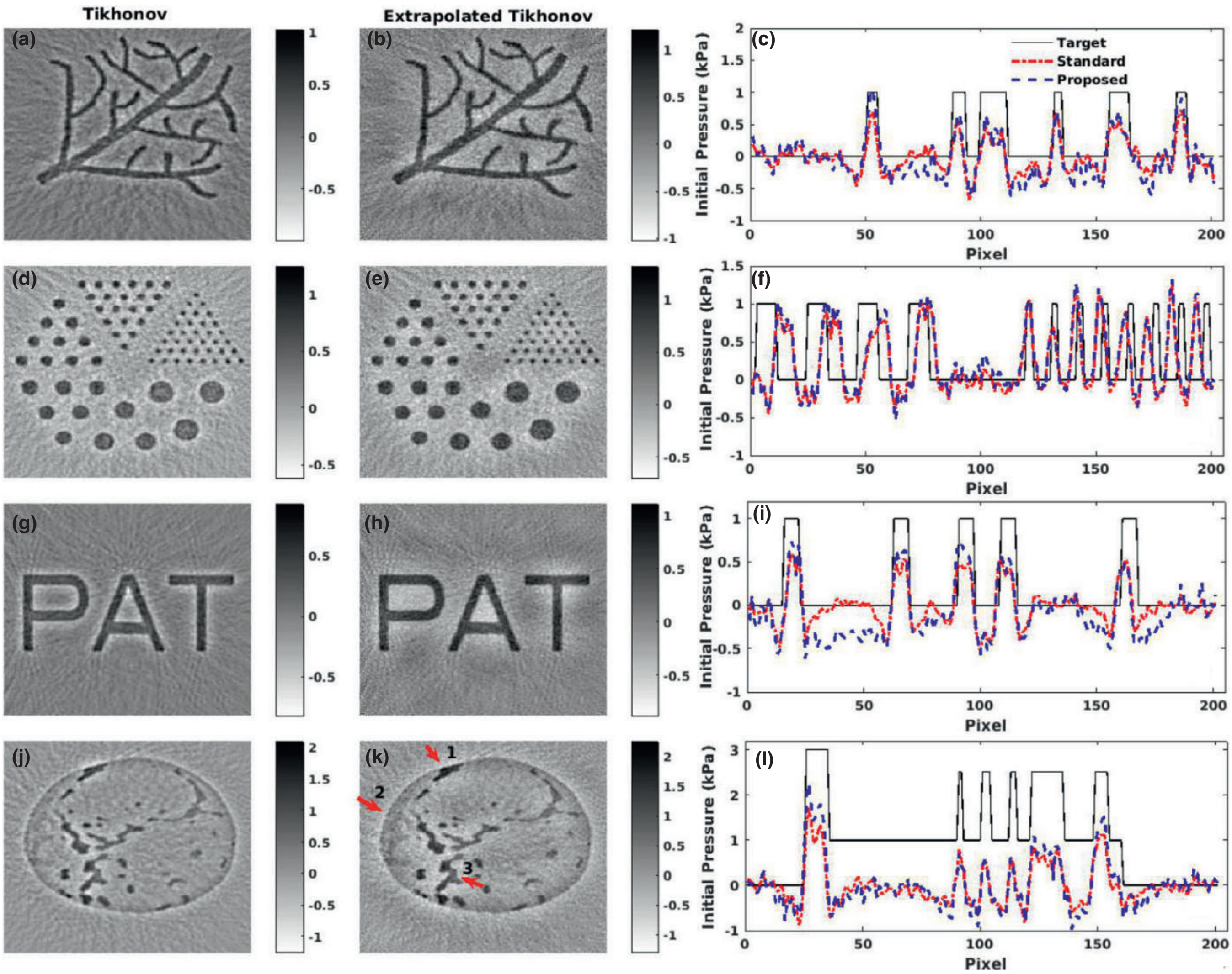

FIG. 7. Reconstructed images for traditional Tikhonov regularization discussed in Section 4.B using error estimate (a,d,g,j) and proposed extrapolated Tikhonov method (b,e,h,k). A one-dimensional profile plot for the reconstructed images along the line in numerical phantoms was shown in (c,f,i,l). The residual norm and performance metrics corresponding to these reconstruction results were given in Fig. 6. [Color figure can be viewed at wileyonlinelibrary.com]

compared to standard error estimate method. The numbered 2 red arrow in Fig. 5(o) shows that the proposed method has better structural visibility than the standard method. The profile plot was shown in Fig. 5(p) and the quantitative metrics were compiled in Fig. 6. In case of the numerical breast phantom, the large difference between the target and the reconstructed initial pressure distribution is due to the limited bandwidth of the transducers utilized to collect the photoacoustic data along with the target dynamic range being much larger compared to other numerical phantoms considered. The regularization parameter determined using the standard error estimate method for the results shown in Figs. 5(b), 5(f), 5(j), 5(n) were 0.0415, 0.0241, 0.0389, and 0.0396, respectively, with q, that is, number of Lanczos iterations being 90.

The results pertaining to blood vessel phantom for Tikhonov method were shown in Figs. 7(a) and 7(b) for error estimate and proposed extrapolated Tikhonov filtering method (discussed in Section 4.B), respectively. The profile plot corresponding to these results was shown in Fig. 7(c). From the results, it was observed that the quantitative accuracy of proposed method was superior to error estimate. The figures of merit (performance metrics) corresponding to the presented results were plotted in Fig. 6. The computational time for the methods discussed were compiled in Table I. It was clearly evident that the proposed method was four times computationally efficient, indicating the effectiveness of the method avoiding the need of computing an appropriate regularization parameter. Similar trend was observed for the Derenzo phantom as shown in Figs. 7(d) and 7(e). Reconstructed results for PAT phantom containing sharp edges were presented in Figs. 7(g) and 7(h). The profile plots corresponding to Derenzo and PAT phantom were shown in Figs. 7(f) and 7(i), respectively. The reconstruction results for realistic breast phantom were shown in Figs. 7(j) and 7(k), along with the profile plot in Fig. 7(l). Similar trend as observed in the case

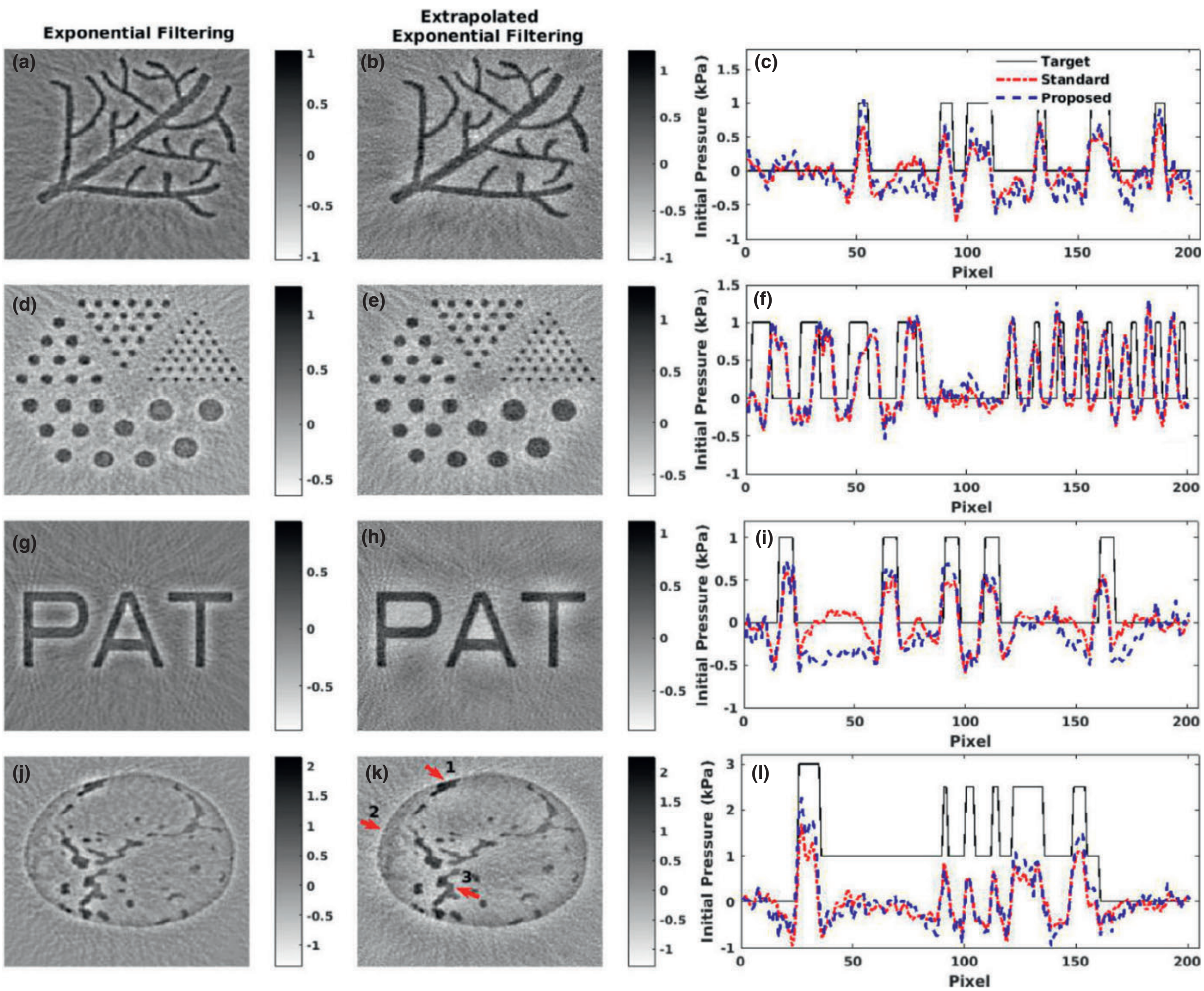

FIG. 8. Reconstructed images for exponential filtering discussed in Section 4.C using error estimate (a,d,g,j) and proposed extrapolated exponential filtering method (b,e,h,k). A one-dimensional profile lot for the reconstructed images along the line in numerical phantoms was shown in (c,f,i,l). The residual norm and performance metrics corresponding to these reconstruction results were given in Fig. 6. [Color figure can be viewed at wileyonlinelibrary.com]

of Tikhonov regularization, being the proposed method has better structural recovery compared to standard method, was indicated by the red arrows in Fig. 7(k). The λ values determined using standard error estimate method for the results presented in Figs. 7(a), 7(d), 7(g), 7(j) were 0.0414, 0.0241, 0.0392, and 0.0400, respectively.

The reconstruction results for exponential filtering using error estimate and proposed exponential filtering method (discussed in Section 4.C) for blood vessel network were shown in Figs. 8(a) and 8(b). The profile plot for the demonstrated results was shown in Fig. 8(c). It was observed that the proposed method performs superior to the standard method in terms of quantitative accuracy. The performance metrics for these results and the residual norm were compiled in Fig. 6. The computational time taken for the methods was given in Table I. Note that for Tikhonov regularization and exponential filtering methods, there is a one-time overhead of computing the SVD of the system matrix, which took 300.7 min. Even in this case, the proposed extrapolation method was four times computationally faster compared to error estimate. The efficiency of the proposed method was that it avoids the need of determining a suitable regularization parameter, which is a computationally expensive process. The results for Derenzo and PAT phantom were shown in Figs. 8(d), 8(e), and 8(g), 8(h), respectively. The profile plots corresponding to these results were shown in Figs. 8(f) and 8(i). The residual norm was given in Fig. 6. From the presented results, it was clearly evident that the same trend has been followed for all the phantoms. The results pertaining to breast phantom were given in Figs. 8(j) and 8(k). The red arrows in Fig. 8(k) indicate the advantages of proposed method over standard technique, being better varying initial pressure reconstruction and structural visibility. The presented results for standard method as shown in Figs. 8(a), 8(d), 8(g), 8(j) were for the λ values 0.0594, 0.0340, 0.0533, and 0.0573, respectively.

The figures of merit for the results discussed till now are given in Fig. 6. From the results, it is clear that the proposed method outperforms rest in terms of all metrics. For results pertaining to Fig. 5(a)–5(c), the universal image quality index (UIQI) for the time-reversal method is 0.017 and for the standard Lanczos Tikhonov method is 0.03, and for the proposed method is 0.08 (providing atleast 2.6 times improvement over standard error estimate method).

The results obtained for experimental horse hair phantom were shown in Fig. 9. Signal-to-noise ratio computed for these results was given below each reconstruction. It was evident from these values that the proposed extrapolated method has around 9 dB better SNR compared to the standard error

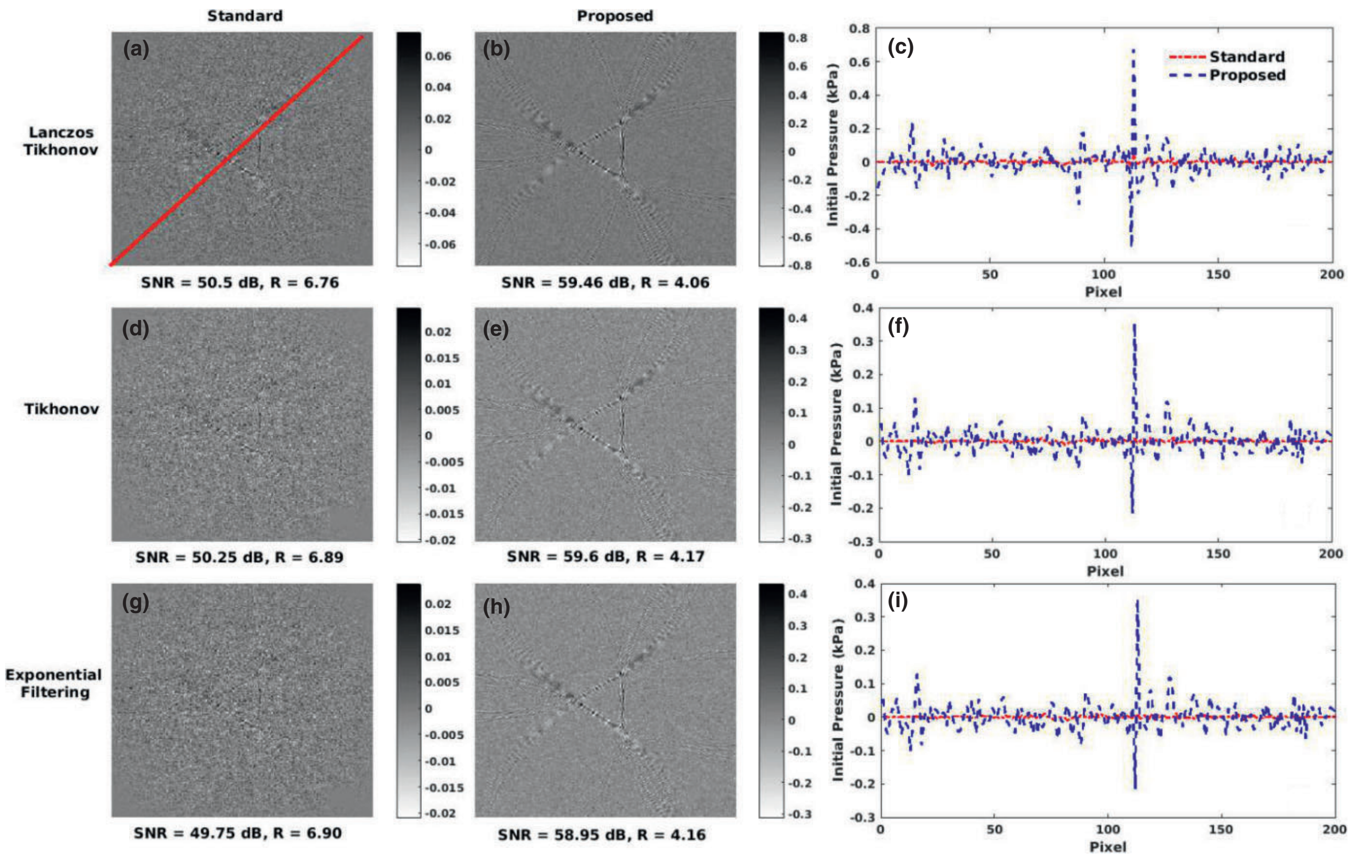

FIG. 9. Reconstructed initial pressure distribution using methods discussed in Section 4 [standard error estimate (a, d, g) and proposed extrapolated method (b, e, h)] with a horse hair phantom (discussed in Section 6.B). The SNR and residue (R) calculated for these reconstructed methods are listed below each image. The higher value of SNR and lower value of R indicates the better performance of reconstruction method. A one-dimensional profile plot for the reconstructed images along the line given in (a) was shown in (c, f, i). The computational time corresponding to these reconstruction results were given in Table I. [Color figure can be viewed at wileyonlinelibrary.com]

estimates method. The computational time taken for these reconstructions was given in Table I. Note that a Linux workstation with 16 cores of Intel Xeon processor having a speed of 2.3 GHz and 256 GB RAM was utilized for experimental phantom data. It should be noted that the proposed method was at least five times faster compared to the standard method.

The reconstructions corresponding to ink-tube phantom were shown in Fig. 10. Signal-to-noise ratio computed for these results were given below each reconstruction. It can be seen from the Fig. 10 that the proposed extrapolation method provides superior performance in terms of reconstruction of structure of tubes. In other words, tubes are better filled in case of proposed method compared to the standard method. A one-dimensional profile plot along the red line in Fig. 10(a) was shown corresponding to each reconstruction to clearly see this effect.

Typically, the sensor geometry in photoacoustic tomography does not enclose the full object, thereby resulting in the limited-view problem. Considering only upper half of detectors (semicircle from 9 'o' clock to 3 'o' clock position in the clockwise direction, making total number of available detectors being 50) for the case of ink-tube phantom, the reconstructed results were shown in Fig. 11. The same trend of better filled circles as seen earlier was also observed here. The one-dimensional profile along the red line shown in Fig. 11(a) was given in the last column of Fig. 11 corresponding to the reconstructions against reach row. The performance metrics SNR and residue were specified below each reconstruction and as seen earlier, the proposed methods provide superior performance even in this case.

8. DISCUSSION

The methods proposed in this work were mainly evaluated using four numerical and two experimental phantoms. The numerical blood vessel phantom with an initial pressure rise of 1 kPa represents the internal blood vessel structures. This phantom mimics the common vasculature imaging scenario applied in photoacoustic imaging. The Derenzo phantom consisting of small and large size initial pressure distributions was also utilized in this work. This phantom represents the capability to image small to large objects (resolution) using the proposed and standard reconstruction methods. To evaluate the methods for reconstructing sharp edges, a target with alphabets "PAT" was considered. All these three phantoms have unipolar pressure distribution. To evaluate methods for varying initial pressure distributions, a realistic breast phantom created from contrast-enhanced magnetic resonance imaging data was considered. The experimental phantoms, horse hair

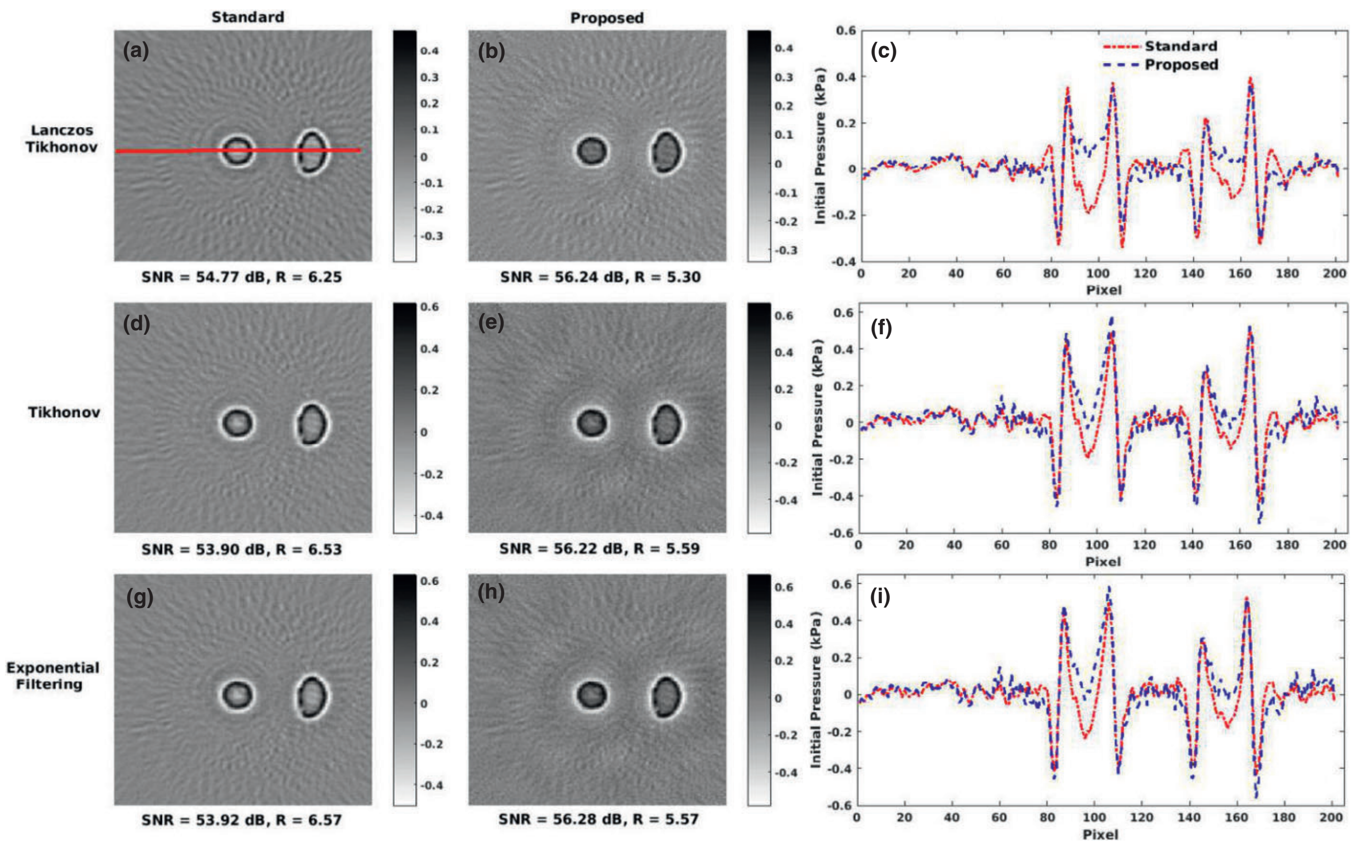

FIG. 10. Reconstructed initial pressure distribution using methods discussed in Section 4 [standard error estimate (a, d, g) and proposed extrapolated method (b, e, h)] with an ink-tube phantom (discussed in Section 4.B). The SNR and residue (R) calculated for these reconstructed methods are listed below each image. The higher value of SNR and lower value of R indicates the better performance of reconstruction method. A one-dimensional profile plot for the reconstructed images along the line given in (a) was shown in (c, f, i). [Color figure can be viewed at wileyonlinelibrary.com]

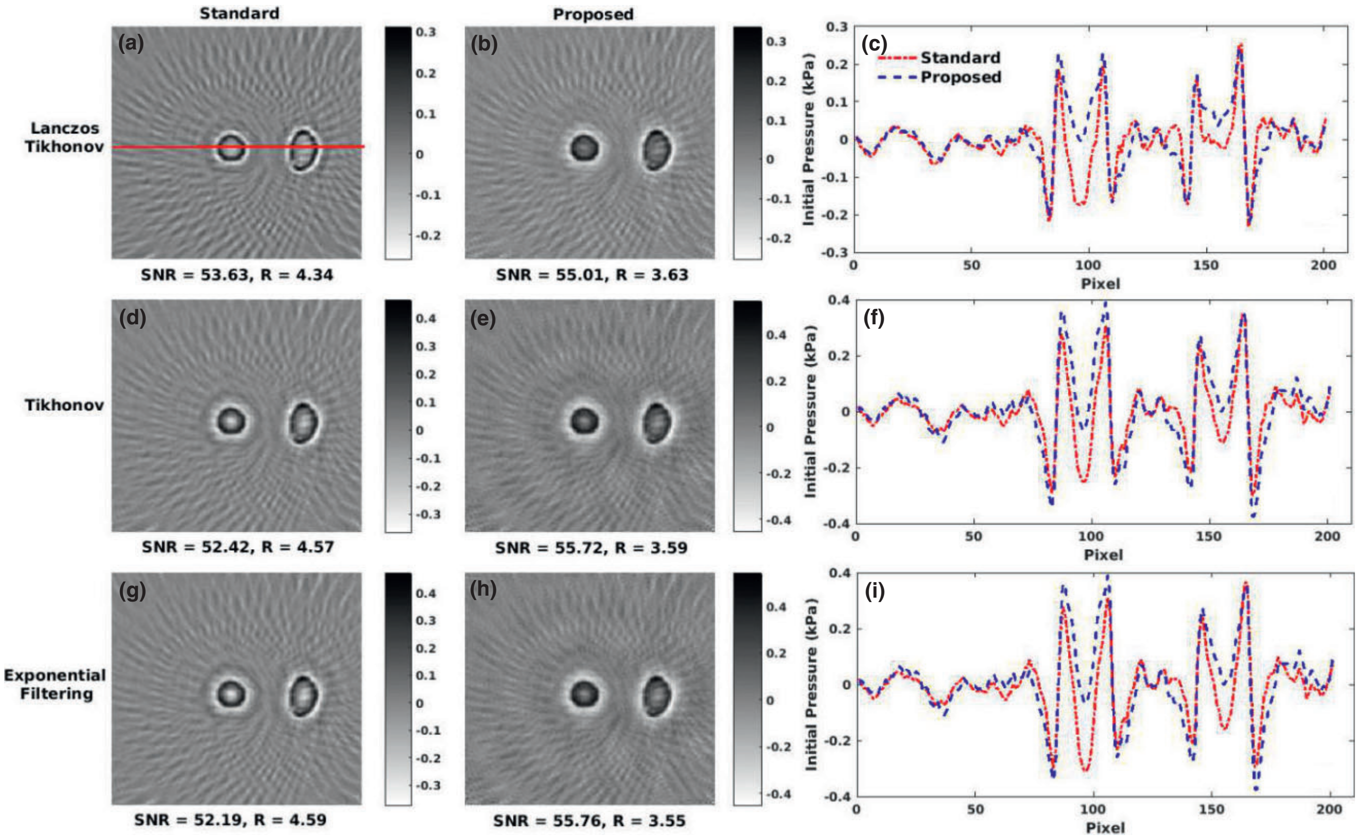

FIG. 11. Reconstructed initial pressure distribution for the limited-view case using methods discussed in Section 4 [standard error estimate (a, d, g) and proposed extrapolated method (b, e, h)] with an ink-tube phantom (discussed in Section 4.B). The SNR and residue (R) calculated for these reconstructed methods are listed below each image. The higher value of SNR and lower value of R indicates the better performance of reconstruction method. A one-dimensional profile plot for the reconstructed images along the line given in (a) was shown in (c, f, i). [Color figure can be viewed at wileyonlinelibrary.com]

and tube phantoms, represent the ability to image high contrast objects that are typically expected in real-time photoacoustic imaging. This controlled experimental data, one representing small objects (horse hair) and another thick objects (ink-tube phantom), was used in this work to evaluate the performance of the proposed algorithms.

The selection of α and β in Eq. (20) is in accordance with the minimum and maximum regularization parameters chosen for the standard error estimate method.[16] From the simulations, we have observed that irrespective of values of α and β, the solution obtained using five λ values was same. Note also that the initial pressure reconstructions using these five λ values can be computed in parallel, thus further reducing the computation time reported in Table I for the proposed extrapolated method. The current limitation of the methods discussed here lies with utilizing the system matrix-based approach. For three-dimensional case, the system matrix size will be large and becomes intractable as the discretization becomes finer. The slice-by-slice reconstruction approach can be applied to recover a three-dimensional volumetric initial pressure distribution.

Figure 12 shows the plot of residual norm [Eq. (35)], error norm ($\|x - x_{recon}\|$), Pearson correlation [Eq. (37)], and contrast to noise ratio [Eq. (38)] for varying range of regularization parameter for both the standard and proposed Tikhonov method corresponding to PAT phantom [Fig. 7(g) and 7(h)]. As the results obtained by the extrapolation method is an approximate solution, there is a discrepancy between the standard and proposed method with standard method errors being lower for all values of λ other than $\lambda = 0$. The proposed method provides significantly improved results in terms of all metrics shown in Fig. 12 at $\lambda = 0$. Note that obtaining solution at $\lambda = 0$ using standard method (equivalent to no regularization) is not plausible due to the ill-conditioned nature of the problem. It is evident from these plots the solution obtained at $\lambda = 0$ (proposed method) provides less errors in terms of residual and error norms along with improved PC and CNR.

Figure 13 shows a plot of residual norm ($\|b - \mathbf{A}x_{recon}\|_2$) vs the number of Lanczos iterations for the result presented in Fig. 5(k). It was observed from the plot that the variation in residual norm becomes insignificant after 25 Lanczos iterations. Therefore, there is no need to determine optimal Lanczos iterations for the proposed method. The standard method [result of Fig. 5(j)] uses error estimate to determine optimal number of Lanczos iterations, and for this case, it was 90. For a fair comparison, the computational time given in Table I for the proposed method was 90 Lanczos iterations. If 25 iterations were utilized instead of 90 iterations, the speedup factor of the proposed method becomes 13 times (as opposed to 4.1 times) in comparison to standard method.

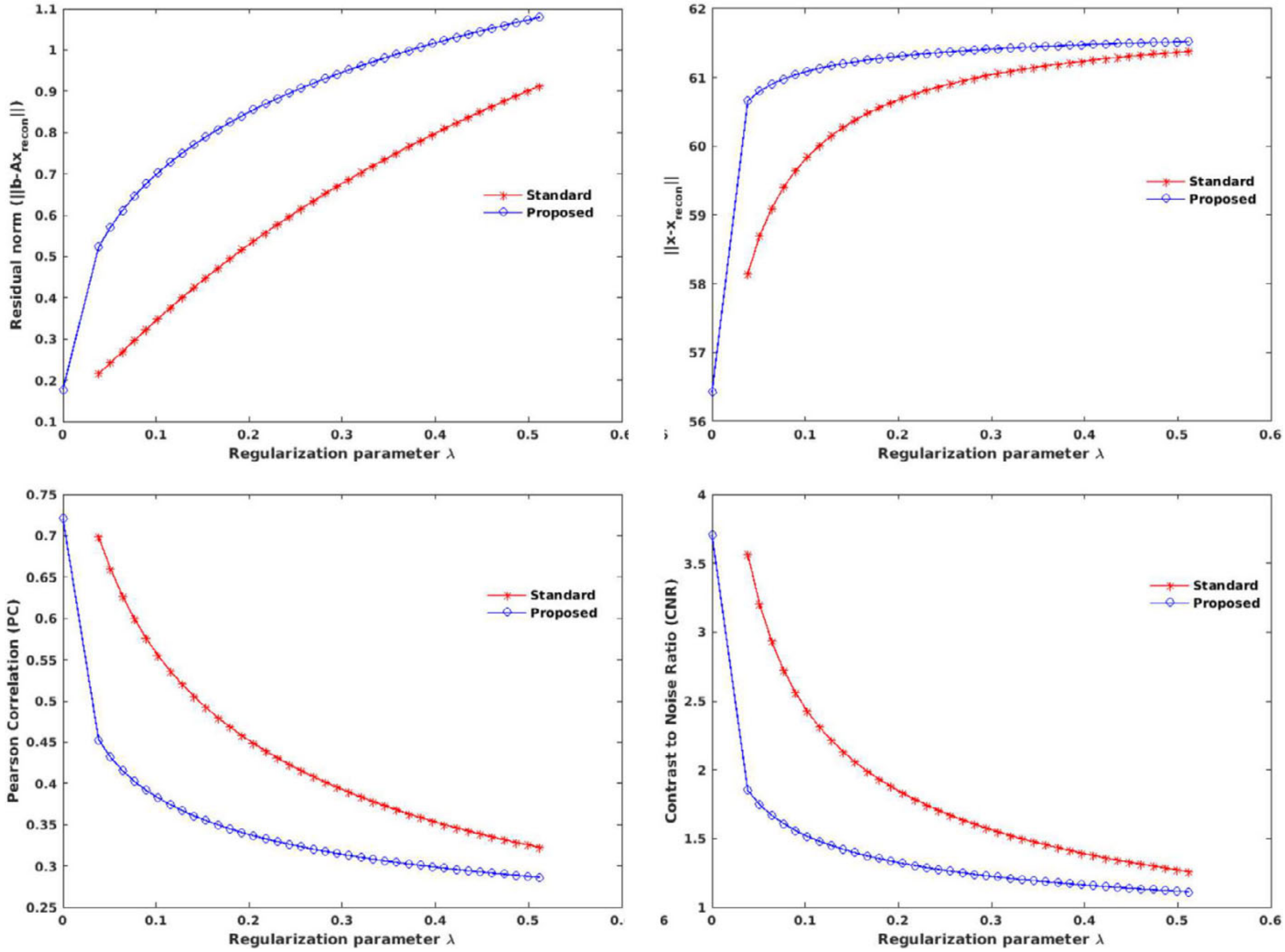

FIG. 12. Plot of residual norm (35), error norm ($\|x - x_{recon}\|$), Pearson correlation (PC) (37), and contrast to noise ratio (CNR) (38) for varying range of regularization parameter for both the standard and proposed Tikhonov method for PAT phantom shown in Figs. 7(g) and 7(h). [Color figure can be viewed at wileyonlinelibrary.com]

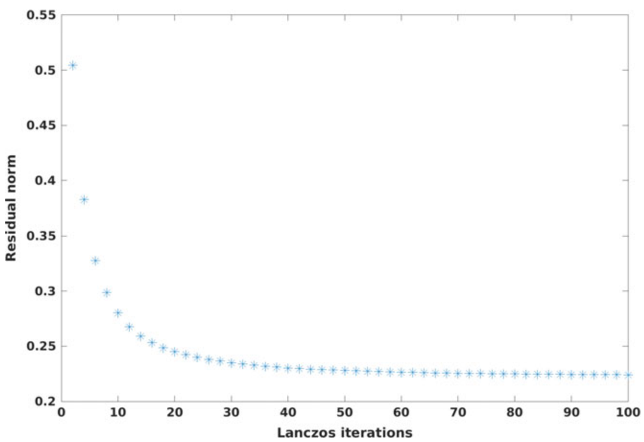

FIG. 13. Plot of the variation of Residual norm [Eq. (35)] using the proposed extrapolated Lanczos Tikhonov method as a function of number of Lanczos iterations for numerical PAT phantom [Fig. 5(k)]. [Color figure can be viewed at wileyonlinelibrary.com]

To estimate the bias, reconstructions using standard and proposed Lanczos Tikhonov methods were performed on a PAT phantom data without adding any noise. The root-mean-squared error in reconstructed initial pressure distribution was found to be 0.2806 and 0.2198 for standard Lanczos Tikhonov and proposed extrapolated Lanczos Tikhonov methods, respectively. This suggests that the proposed extrapolated method has less bias compared to the standard error estimates method.

It is evident from Fig. 6 that the proposed extrapolated method was able to perform better than the earlier standard error estimate method in three different regularization frameworks with an added advantage of proposed method being computationally efficient (Table I). The simplicity of the proposed method does not compromise the reconstructed image quality and in fact, as stated earlier, provides better image characteristics in realistic breast phantom case.

Note that even though the attempt here was to find the solution corresponding to $\lambda = 0$ via the extrapolation scheme, the method is generic enough to find the solution at any other λ value.[24] For example, if one finds the λ using Lanczos Tikhonov method as detailed in,[22] the solution can be found at that particular λ using this scheme. The solution at $\lambda = 0$ will have the best resolution characteristics (evidenced by Fig. 12 also), as the regularization is known to blur the reconstructed image[17,18] and this will give an estimate of deblurred reconstructed image.

The inherent limitation of this method is that it relies on utilization of solution obtained at various values of λ. These λ values have to be separated reasonably [as chosen via Eq. (20)] and obtaining these solutions requires one to perform either computationally expensive SVD of system matrix or utilize the solution via equivalent of [Eq. (6)]. This, in general, requires number of operations being $O(n^3)$ or higher. Furthermore, due to the discrepancy between the extrapolated solution and standard method (please see Fig. 12) obtaining solution other than $\lambda = 0$ may not be worthwhile using the proposed method as the solution is only an approximation to the expected one at all other λ values.

It is important to note that the extrapolated method has been implemented in the Tikhonov filtering framework (with three of such variants presented in here, namely Lanczos Tikhonov, traditional Tikhonov, and exponential filtering) and proven that it provides solutions that are less biased to regularization. The extrapolated method is also very generic in nature, it can be extended to other regularization schemes, which use nonsmooth regularizers (like ℓ_1 or total variation based), as long the minimization results are available for large number of regularization parameter realizations. In simple terms, one need to compute solutions for more than five λ values. Computing these solutions for large realizations of λ (regularization parameter) values might not be providing any competitive advantage in terms of computational efficiency compared to the error estimate method proposed earlier[16] for nonsmooth regularization schemes.

The error estimate method is inherently a sequential method, which requires the previous iteration as an input to determine the current iteration results and parallelizing this method using General Purpose-Graphics Processing Units (GP-GPUs) may not be providing significant speedup and the same is true with most methods (including GCV and Minimal Residual Method[22]). Thus, obtaining fourfold speedup with the proposed method (with exclusion of estimating the regularization parameter) is a significant reduction in computational time. Moreover, the reconstruction results obtained using proposed method are superior compared to standard methods, such as error estimate (please refer to Figs. 6, 9, 10, 11, and 12).

9. CONCLUSION

Model-based reconstruction techniques were shown to be effective in limited data cases, providing better quantitative accuracy. These model-based reconstruction schemes often utilize regularization to provide meaningful results and an automated choice of regularization is often considered as a computationally demanding procedure. Moreover, among these model-based techniques, the standard Tikhonov filtering techniques assume that the expected acoustic image is smooth and piecewise constant, thus making the reconstructed image with regularization loose sharp features. In this work, a simple and effective extrapolation technique was proposed that provides the solution at $\lambda = 0$, mitigating the effect of blur induced by the regularization as well as removing the necessity of computing regularization parameter. It was shown with numerical as well as experimental phantom data that the proposed method is superior in terms of providing quantitatively accurate reconstructions and is atleast four times computationally efficient compared to earlier proposed error estimate method that evaluates the regularization parameter in an automated fashion.

ACKNOWLEDGMENTS

This work was supported by the Department of Biotechnology (DBT) Innovative Young Biotechnologist Award (IYBA) (No.: BT/07/IYBA/2013-13) and DBT Bioengineering Grant (No.: BT/PR7994/ MED/32/ 284/2013). The authors acknowledge financial support from the Tier 1 grant funded by the Ministry of Education in Singapore (RG48/16: M4011617), and the Singapore National Research Foundation administered by the Singapore Ministry of Healths National Medical Research Council (NMRC/OFIRG/0005/2016: M4062012).

CONFLICTS OF INTEREST

There are no conflicts of interest declared by Authors.

APPENDIX A

EXTRAPOLATED SOLUTION WITHOUT THE NEED OF COMPUTING THE SVD

The closed-form regularized Tikhonov solution can be expressed as

$$x_{\lambda_j} = (\mathbf{A}^T\mathbf{A} + \lambda_j\mathbf{I})^{-1}\mathbf{A}^T b. \tag{41}$$

where $j = 1,2...p$ with p denoting the total number of λ values. Rearranging the above expression, we obtain:

$$(\mathbf{A}^T\mathbf{A} + \lambda_j\mathbf{I})x_{\lambda_j} = \mathbf{A}^T b. \tag{42}$$

Summing the above equation for all values of j with p defined as in Eq. (14),

$$\frac{1}{p}\left[\sum_{j=1}^{p}(\mathbf{A}^T\mathbf{A} + \lambda_j\mathbf{I})x_{\lambda_j}\right] = \mathbf{A}^T b. \tag{43}$$

$$\left(\mathbf{A}^T\mathbf{A}\sum_{j=1}^{p} x_{\lambda_j}\right) + \sum_{j=1}^{p}\lambda_j x_{\lambda_j} = p\mathbf{A}^T b. \tag{44}$$

Multiplying with $x_{\lambda_j}^T$ on both sides toward the right of Eq. (44) results in

$$\mathbf{A}^T\mathbf{A}\left(\sum_{j=1}^{p} x_{\lambda_j}\right)x_{\lambda_j}^T + \left(\sum_{j=1}^{p} \lambda_j x_{\lambda_j}\right)x_{\lambda_j}^T = \left(p\mathbf{A}^T b\right)x_{\lambda_j}^T. \quad (45)$$

Solving the Eq. (45) for $\mathbf{A}^T\mathbf{A}$, we obtain

$$\mathbf{A}^T\mathbf{A} = \left(p\mathbf{A}^T b x_{\lambda_j}^T - \left(\sum_{j=1}^{p} \lambda_j x_{\lambda_j}\right)x_{\lambda_j}^T\right)\left(\left(\sum_{j=1}^{p} x_{\lambda_j}\right)x_{\lambda_j}^T\right)^{-1}. \quad (46)$$

The solution at $\lambda = 0$ is obtained by substituting Eq. (46) in Eq. (41),

$$\begin{aligned} x^e &= \left[\left(p\mathbf{A}^T b x_{\lambda_j}^T - \left(\sum_{j=1}^{p} \lambda_j x_{\lambda_j}\right)x_{\lambda_j}^T\right)\left(\left(\sum_{j=1}^{p} x_{\lambda_j}\right)x_{\lambda_j}^T\right)^{-1}\right]^{-1}\mathbf{A}^T b \\ &= \left[\left(p\mathbf{A}^T b - \sum_{j=1}^{p} \lambda_j x_{\lambda_j}\right)\left(\sum_{j=1}^{p} x_{\lambda_j}\right)^{-1}\right]^{-1}\mathbf{A}^T b \\ &= \left(\sum_{j=1}^{p} x_{\lambda_j}\right)\left(p\mathbf{A}^T b - \sum_{j=1}^{p} \lambda_j x_{\lambda_j}\right)^{-1}\mathbf{A}^T b \\ &= \left(\sum_{j=1}^{p} x_{\lambda_j}\right)\frac{\left(p\mathbf{A}^T b - \sum_{j=1}^{p} \lambda_j x_{\lambda_j}\right)^T}{|(p\mathbf{A}^T b - \sum_{j=1}^{p} \lambda_j x_{\lambda_j})|^2}\mathbf{A}^T b. \end{aligned} \quad (47)$$

where e in the superfix denotes the extrapolated solution at $\lambda = 0$.

APPENDIX B

COMPARISON OF SOLUTIONS OBTAINED USING LEAST SQUARES, TIKHONOV, AND EXTRAPOLATED TIKHONOV METHODS:

The unregularized least-squares problem [same as Eq. (3)] minimizes the following objective function with respect to x:

$$\Gamma = \|\mathbf{A}x - b\|_2^2, \quad (48)$$

where $\mathbf{A}$ is the system matrix and x represents the parameter of interest (initial pressure distribution). The least-squares solution (from normal equations) for Eq. (48) is

$$x_{LS} = (\mathbf{A}^T\mathbf{A})^{-1}\mathbf{A}^T b = \mathbf{A}^\dagger b \quad (49)$$

where $\mathbf{A}^\dagger$ denotes the Moore-Penrose pseudo inverse of $\mathbf{A}$. The measured data b can be represented as $b = \bar{b} + \xi$, with $\bar{b}$ corresponding to the noise-free measurement and ξ as the noise in the data. Rewriting Eq. (49) results in

$$x_{LS} = \mathbf{A}^\dagger\bar{b} + \mathbf{A}^\dagger\xi = \bar{x} + \epsilon_{LS} \quad (50)$$

where $\bar{x}$ represents the noise free solution and $\varepsilon_{LS} = \mathbf{A}^\dagger\xi$ represents the inverse noise in the reconstructed solution. The unregularized least-squares solution in terms of SVD can be written as:

$$x_{LS} = \sum_{i=1}^{k}\frac{<U_i, \bar{b}>}{S_i}V_i + \sum_{i=1}^{k}\frac{<U_i, \xi>}{S_i}V_i. \quad (51)$$

For an ill-conditioned system (like the one at hand), the singular values are either small ($S_i \to 0$) or the system has high condition number (the ratio of maximum to minimum singular value $\frac{S_{max}}{S_{min}} \to \infty$). In this case, $x_{LS} \to \infty$ as $1/S_i \to \infty$.

Regularization aims at reducing the inverse noise, where the Eq. (48) is replaced with a nearby problem whose solution is less sensitive to noise ξ. The resultant cost function, which also known as Tikhonov regularization, becomes:

$$\gamma = \|\mathbf{A}x - b\|_2^2 + \lambda\|x\|_2^2, \quad (52)$$

where λ is the regularization parameter and is strictly greater than zero ($\lambda > 0$). The solution of Eq. (52) can be expressed using normal equations as:

$$x_{Tik} = (\mathbf{A}^T\mathbf{A} + \lambda I)^{-1}\mathbf{A}^T b. \quad (53)$$

If λ is too high, the algorithm penalizes the solution spaces (removing all high-frequency components), resulting in over-smoothing. Lower value of λ leads to the reconstructed image to have more inverse noise (but retains high-frequency components). Thus, the choice of λ dictates the reconstructed image characteristics. The Tikhonov solution in terms of SVD can be expressed as:

$$\begin{aligned} x_{Tik} &= \sum_{i=1}^{k}\frac{S_i^2}{S_i^2 + \lambda}\frac{<U_i, \bar{b}>}{S_i}V_i \\ &+ \sum_{i=1}^{k}\frac{S_i^2}{S_i^2 + \lambda}\frac{<U_i, \xi>}{S_i}V_i. \end{aligned} \quad (54)$$

Regularization adjusts the filter factors ($F_i = \frac{S_i^2}{S_i^2+\lambda}$) by damping the solution for cases $S_i \to 0$. The filter factors $F_i \to 1$ for singular values much larger than λ and $F_i \to 0$ for singular values much smaller than λ. Note that when $\lambda = 0$, the solution of unregularized least squares [Eq. (49)] and Tikhonov solutions [Eq. (53)] become equal.

The extrapolated solution at $\lambda = 0$ in terms of SVD for the Tikhonov regularization case [Eq. (28)] is:

$$x_{Tik}^e = \sum_{i=1}^{k}\frac{1}{p} < \sum_{j=1}^{p}\left(1 + \frac{\lambda_j}{S_i^2}\right)x_{\lambda_j}, V_i > V_i, \quad (55)$$

where e in the super fix denotes the extrapolated solution at $\lambda = 0$. It is important to note that the extrapolated solution depends only on the regularized least-squares solutions (x_{λ_j}) computed at predefined values of regularization parameters (λ_j). The tables given below showcase the solution characteristics for the methods discussed in this Appendix, mainly highlighting the case of $\lambda = 0$.

From Tables-II and III, it is very clear that the least-squares solution (x_{LS}) does not even exist for the ill-conditioned system. The Tikhnov regularization demands $\lambda > 0$ for an ill-conditioned system, essentially computing of x_{Tik}

TABLE II. The existence of solution for ill-conditioned and well-conditioned systems.

$\lambda = 0$	Least squares x_{LS} [Eq. (51)]	Tikhonov x_{Tik} [Eq. (54)]	Extrapolation x^e_{Tik} [Eq. (55)]
Ill-conditioned systems (the problem at hand)	Solution does not exist	Not applicable as $\lambda > 0$	Approximates the solution at $\lambda = 0$
Well-conditioned systems	Solution exists	Regularization is not required, so not applicable	Not applicable

TABLE III. The behavior of the solution for the ill-conditioned systems, such as problem at hand.

Condition	Least squares x_{LS} [Eq. (51)]	Tikhonov x_{Tik} [Eq. (54)]	Extrapolation x^e_{Tik} [Eq. (55)]	
			x^e_{Tik} [Eq. (55)]	Remarks
$S_i \to 0$	$\to\infty$	$\to 0$	$\to 0$	as $x_{\lambda_j} \to 0$
$\frac{S_{max}}{S_{min}} \to \infty$	$\to\infty$	For $\lambda > 0$, solution is bounded	depends on x_{λ_j} & λ_j	Numerical approximation based on extrapolation for $\lambda = 0$

with $\lambda = 0$ case same as least-squares case, where the solution does not exist. The only way to compute the solution via numerical approximation for the case of $\lambda = 0$ is to use extrapolated Tikhonov (x^e_{Tik}), which depends only on the precomputed Tikhonov solutions (x_{λ_j} with $\lambda_j > 0$).

[a]Author to whom correspondence should be addressed. Electronic mail: yalavarthy@iisc.ac.in.

REFERENCES

1. Wang LV, Hu S. Photoacoustic tomography: in vivo imaging from organelles to organs. *Science*. 2012;335:1458–1462.
2. Li L, Zhu L, Ma C, et al. Single-impulse panoramic photoacoustic computed tomography of small-animal whole body dynamics at high spatiotemporal resolution. *Nat Biomed Eng*. 2017;1:0071.
3. Razansky D, Kellnberger S, Ntziachristos V. Near-field radiofrequency thermoacoustic tomography with impulse excitation. *Med Phys*. 2010;37:4602–4607.
4. Upputuri PK, Pramanik M. Recent advances towards preclinical and clinical translation of photoacoustic tomography: a review. *J Biomed Opt*. 2017;22:041006.
5. Hu S. Listening to the brain with photoacoustics. *IEEE J Sel Topics Quant Electr*. 2016;22:6800610.
6. Li CH, Wang LV. Photoacoustic tomography of the mouse cerebral cortex with a high-numerical-aperture-based virtual point detector. *J Biomed Opt*. 2009;14:024047.
7. Upputuri PK, Pramanik M. Dynamic in vivo imaging of small animal brain using pulsed laser diode based photoacoustic tomography system. *J Biomed Opt*. 2017;22:090501.
8. Xu Y, Wang LV. Rhesus monkey brain imaging through intact skull with thermoacoustic tomography. *IEEE Trans Ultrason Ferroelectr Freq Control*. 2006;53:542–548.
9. Li X, Heldermon CD, Yao L, Xi L, Jiang H. High resolution functional photoacoustic tomography of breast cancer. *Med Phys*. 2015;42:5321–5328.
10. Hoelen CGA, De Mul FFM, Pongers R, Dekker A. Three-dimensional photoacoustic imaging of blood vessels in tissue. *Opt Lett*. 1998;23:648–650.
11. Li CH, Wang LHV. Photoacoustic tomography and sensing in biomedicine. *Phys Med Biol*. 2009;54:R59–R97.
12. Siphanto RI, Thumma KK, Kolkman RGM, et al. Serial noninvasive photoacoustic imaging of neovascularization in tumor angiogenesis. *Opt Express*. 2005;13:89–95.
13. Rosenthal A, Ntziachristos V, Razansky D. Acoustic inversion in optoacoustic tomography: a review. *Curr Med Imaging Rev*. 2013;9:318–336.
14. Zhou Y, Yao J, Wang LV. Tutorial on photoacoustic tomography. *J Biomed Opt*. 2016;21:061007.
15. Xu Y, Wang LV, Ambartsoumian G, Kuchment P. Reconstructions in limited view thermoacoustic tomography. *Med Phys*. 2004;31:724–733.
16. Bhatt M, Acharya A, Yalavarthy PK. Computationally efficient error estimate for evaluation of regularization in photoacoustic tomography. *J Biomed Opt*. 2016;21:106002.
17. Prakash J, Dehghani H, Pogue BW, Yalavarthy PK. Model resolution based basis pursuit deconvolution improves diffuse optical tomographic imaging. *IEEE Trans Med Imaging*. 2014;33:891–901.
18. Prakash J, Raju AS, Shaw CB, Pramanik M, Yalavarthy PK. Basis pursuit deconvolution for improving model-based reconstructed images in photoacoustic tomography. *Biomed Opt Express*. 2014;5:1363–1377.
19. Morozov VA. *Methods for Solving Incorrectly Posed Problems*. New York: Springer Science & Business Media; 2012.
20. Wahba G, Craven P. Smoothing noisy data with spline functions: estimating the correct degree of smoothing by the method of generalized cross validation. *Numer Math*. 1978;31:377–404.
21. Hansen PC, O'Leary DP. The use of the L-curve in the regularization of discrete ill-posed problems. *SIAM J Sci Comput*. 1993;14:1487–1503.
22. Shaw CB, Prakash J, Pramanik M, Yalavarthy PK. Least squares QR-based decomposition provides an efficient way of computing optimal regularization parameter in photoacoustic tomography. *J Biomed Opt*. 2013;18:080501.
23. Brezinski C, Redivo-Zaglia M, Rodriguez G, Seatzu S. Extrapolation techniques for ill-conditioned linear systems. *Numer Math*. 1998;81:1–29.
24. Rodriguez G, Seatzu S, Theis D. A new technique for ill-conditioned linear systems. *Numer Algorithms*. 2003;33:433–442.
25. Okawa S, Hirasawa T, Kushibiki T, Ishihara M. Numerical evaluation of linearized image reconstruction based on finite element method for biomedical photoacoustic imaging. *Opt Rev*. 2013;20:442–451.
26. Sheu YL, Li PC. Simulations of photoacoustic wave propagation using a finite-difference time-domain method with Berenger's perfectly matched layers. *J Opt Soc Am A*. 2008;124:3471–80.
27. Treeby BE, Cox BT. k-Wave: MATLAB toolbox for the simulation and reconstruction of photoacoustic wavefields. *J Biomed Opt*. 2010;15:021314.
28. Galetti E, Halliday D, Curtis A. A simple and exact acoustic wavefield modeling code for data processing, imaging, and interferometry applications. *Geophysics* 2013;78:F17–F27.
29. Bhatt M, Gutta S, Yalavarthy PK. Exponential filtering of singular values improves photoacoustic image reconstruction. *J Opt Soc Am A*. 2016;33:1785–1792.
30. Paige CC, Saunders MA. LSQR: an algorithm for sparse linear equations and sparse least squares. *ACM Trans Math Softw*. 1982;8:43–71.

31. Larsen RM. Lanczos bidiagonalization with partial reorthogonalization. *DAIMI Report Series*. 1998. https://doi.org/10.7146/dpb.v27i537.7070
32. Reichel L, Rodriguez G, Seatzu S. Error estimates for large-scale ill-posed problems. *Numer Algorithm.* 2009;51:341–361.
33. Brezinski C, Rodriguez G, Seatzu S. Error estimates for the regularization of least squares problems. *Numer Algorithm*. 2009;51:61–76.
34. Hansen PC. Regularization tools version 4.0 for Matlab 7.3. *Numer Algorithms*. 2007;46:189–194.
35. Prakash J, Shaw CB, Manjappa R, Kanhirodan R, Yalavarthy PK. Sparse recovery methods hold promise for diffuse optical tomographic image reconstruction. *IEEE J Sel Top Quantum Electr*. 2014;20:74–82.
36. Wang Z, Bovik AC. A universal image quality index. *IEEE Sig Process Lett*. 2002;9:81–84.
37. Lou Y, Mitsuhashi K, Appleton CM, Oraevsky A, Anastasio MA. Generation of anatomically realistic numerical phantoms for optoacoustic breast imaging. *Proc SPIE* 2016;9708:970840.
38. Lou Y, Zhou W, Matthews TP, Appleton CM, Anastasio MA. Generation of anatomically realistic numerical phantoms for photoacoustic and ultrasonic breast imaging. *J Biomed Opt.* 2017;22:041015.
39. Kalva SK, Pramanik M. Experimental validation of tangential resolution improvement in photoacoustic tomography using a modified delay-and-sum reconstruction algorithm. *J Biomed Opt.* 2016;21:086011.
40. American National Standards Institute. *American National Standard for the Safe Use of Lasers in Health Care Facilities.Standard Z136.1-2000*. New York: ANSI; 2000.
41. Upputuri PK, Pramanik M. Pulsed laser diode based optoacoustic imaging of biological tissues. *Biomed Phys Eng Expr*. 2015;1:045010.